# Evolution of serpentinite from seafloor hydration to subduction zone metamorphism: Petrology and geochemistry of serpentinite from the ultrahigh pressure North Qaidam orogen in nor…

**Article** *in* Lithos · July 2019

DOI: 10.1016/j.lithos.2019.105158

CITATIONS
0

READS
261

**3 authors**, including:

Long Zhang
Guangzhou Institute of Geochemistry
**8** PUBLICATIONS **99** CITATIONS
SEE PROFILE

Ren-Xu Chen
University of Science and Technology of China
**49** PUBLICATIONS **2,150** CITATIONS
SEE PROFILE

Lithos 346–347 (2019) 105158

Contents lists available at ScienceDirect

Lithos

journal homepage: www.elsevier.com/locate/lithos

# Evolution of serpentinite from seafloor hydration to subduction zone metamorphism: Petrology and geochemistry of serpentinite from the ultrahigh pressure North Qaidam orogen in northern Tibet

Long Zhang [a,*], Wei-dong Sun [b,c,d], Ren-Xu Chen [e]

[a] CAS Key Laboratory of Mineralogy and Metallogeny, Guangzhou Institute of Geochemistry, Chinese Academy of Sciences, Guangzhou 510640, China
[b] Center of Deep Sea Research, Institute of Oceanology, Chinese Academy of Sciences, Qingdao 266071, China
[c] Laboratory for Marine Mineral Resources, Qingdao National Laboratory for Marine Science and Technology, Qingdao 266237, China
[d] CAS Center for Excellence in Tibetan Plateau Earth Sciences, Chinese Academy of Science, Beijing 100101, China
[e] CAS Key Laboratory of Crust-Mantle Materials and Environments, School of Earth and Space Sciences, University of Science and Technology of China, Hefei 230026, China

ARTICLE INFO

*Article history:*
Received 21 December 2018
Received in revised form 19 July 2019
Accepted 26 July 2019
Available online 31 July 2019

*Keywords:*
Serpentinite
Lizardite
Antigorite
Subduction
Fluid-mobile elements
North Qaidam

ABSTRACT

Serpentinite from the North Qaidam ultrahigh pressure metamorphic belt in northern Tibet is studied to provide insight into petro-geochemical evolution of serpentinite from seafloor hydration to subduction zone metamorphism. The North Qaidam serpentinite can be divided into undeformed lizardite serpentinite that was not severely overprinted during subduction and deformed antigorite serpentinite that was well recrystallized during subduction. Petrological and geochemical analyses demonstrate that the serpentinite was originally melt-percolated refractory abyssal harzburgite. Considering the local geodynamic setting, it is inferred that the serpentinite probably originated from the oceanic lithosphere that subducted before continental subduction. Relatively uniform low $\delta^{18}O$ (4.0‰–4.5‰) of the antigorite serpentinite indicates high temperature hydrothermal alteration of protolith harzburgite by seawater. In contrast, much lower $\delta^{18}O$ (0.6‰–2.7‰) of the lizardite serpentinite is ascribed to exchange with meteoric water at the Earth's surface. Relict serpentinization textures are well preserved in the lizardite serpentinite, with reactions of olivine to lizardite and magnetite, pyroxenes to talc, tremolite, and lizardite, and spinel to chromite and chlorite. The replacement of lizardite by antigorite during subduction mostly initiates along grain boundaries and interconnecting veinlets, implying fluid-assisted transformation of lizardite into antigorite. Partial decomposition of antigorite produces magnesian secondary olivine in the antigorite serpentinite, while direct breakdown of metastable lizardite generates ferroan secondary olivine in the lizardite serpentinite. The serpentinite is enriched in fluid-mobile elements, with U primarily accumulated during seafloor alteration and alkalis notably introduced by sedimentary fluids at bending faults or in accretionary wedge. Infiltration by fluids equilibrated with sediments is also supported by highly elevated $^{87}Sr/^{86}Sr$ of the serpentinite. Moreover, $^{87}Sr/^{86}Sr$ of the antigorite serpentinite (0.710649–0.713996) is higher than that of the lizardite serpentinite (0.707184–0.708502), which implies more intense interaction of sedimentary fluids with the former than the latter. However, the lizardite serpentinite contains more alkalis and less U than the antigorite serpentinite, which indicates that large proportions of alkalis were lost during partial dehydration of serpentinite, while U was not released.



## 1. Introduction

Recent studies have highlighted the role of serpentinite as a prominent reservoir for volatiles and fluid-mobile elements (FME) in subduction zones (Alt et al., 2013; Deschamps et al., 2013; Evans et al., 2013). Compared with hydrous minerals in subducted oceanic crust and sediments, hydrous minerals in subducted serpentinite can persist to subarc depth and dominate the deep fluid cycle in subduction zones (Rüpke et al., 2004; Schmidt and Poli, 1998; Ulmer and Trommsdorff, 1995; Wunder and Schreyer, 1997). Fluids produced during deserpentinization can boost element release and partial melting in subducted oceanic slab and finally contribute to arc magma generation (Spandler and Pirard, 2013). Moreover, serpentinite can prevail over oceanic crust and sediments in some volatiles and FME (Alt et al., 2013; Deschamps et al., 2013; Kodolányi et al., 2012; Spandler et al., 2014), and geochemical studies have revealed convincing evidence for serpentinite-derived fluid components in some arc lavas (Scambelluri and Tonarini, 2012; Singer et al., 2007; Tonarini et al., 2011). In this regard, revealing the petrological and geochemical evolution of subducted

* Corresponding author.
*E-mail address:* zhanglong@gig.ac.cn (L. Zhang).

https://doi.org/10.1016/j.lithos.2019.105158
0024-4937/

serpentinite is important for the understanding of fluid activity, element recycling, and arc magmatism in subduction zones.

Serpentinite is a common lithology in high-pressure (HP) to ultrahigh-pressure (UHP) orogenic belts. Chemical composition and primary serpentinization sequence of subducted serpentinite can vary greatly due to diverse protolith nature and hydration conditions. During subduction, serpentinite undergoes gradual metamorphism that leads to changes in mineral assemblage and element budgets. The three most remarkable metamorphic stages in subducted serpentinite are transformation of lizardite/chrysotile into antigorite, appearance of secondary olivine, and ultimately complete decomposition of antigorite (Evans, 2004; Scambelluri et al., 2004a). Release of FME is suggested for subducted serpentinite during these dehydration reactions, although the exact behavior of FME during each dehydration episode is not straightforward (Debret et al., 2013a; Deschamps et al., 2013; Kodolányi and Pettke, 2011; Lafay et al., 2013; Scambelluri et al., 1997, 2001, 2004b, 2015). Nevertheless, studies on subducted serpentinite mostly reveal significant enrichment instead of depletion in some FME, which is ascribed to interaction with fluids equilibrated with sediments (Barnes et al., 2014; Cannaò et al., 2015, 2016; Deschamps et al., 2010, 2011, 2012, 2013; Lafay et al., 2013; Marchesi et al., 2013). Therefore, serpentinite can act as either a source or a sink for FME in subduction zones, depending on metamorphic conditions and availability of sedimentary fluids (Deschamps et al., 2010, 2013; Lafay et al., 2013). Overall, petrological evolution and accompanying behaviors of FME in subducted serpentinite are far from well-understood.

The North Qaidam orogen is an Early Paleozoic UHP metamorphic belt that consists of both continental and oceanic materials in northern Tibet (Song et al., 2014). Sporadic serpentinite blocks, hosted either in oceanic eclogite or in continental gneiss, occur in eastern segment of the UHP belt (Song et al., 2009; Zhang et al., 2008). The serpentinite preserves typical textures of relict mantle paragenesis, serpentinization reactions, and phase transformations related to subduction (Song et al., 2009; Zhang et al., 2008). In this study, petrological and geochemical data are presented for serpentinite from the Shaliuhe area of the North Qaidam orogen. The results are used to constrain the protolith nature, metamorphic petrology, and element budgets of the North Qaidam serpentinite, providing insight not only into the tectonics of the North Qaidam orogen, but also into the general petro-geochemical evolution of serpentinite from seafloor hydration to subduction zone metamorphism.

## 2. Geological setting and samples

The North Qaidam orogen, located in northeastern Tibetan Plateau (Fig. 1a), is a typical continental-type UHP metamorphic belt formed by deep subduction and exhumation of the Qaidam block beneath the Qilian block (Song et al., 2014; Zhang et al., 2017a). It extends discontinuously in a northwest-southeast trend for about 400 km between the Qaidam block and the Qilian block (Fig. 1a). UHP metamorphic rocks crop out in four subunits from the southeast to northwest: the Dulan terrane, the Xitieshan terrane, the Lüliangshan terrane, and the Yuka terrane (Fig. 1a). The UHP metamorphic zone is mainly composed of granitic and pelitic gneiss with subordinate enclosed eclogite, granulite, and ultramafic rocks (Song et al., 2014; Zhang et al., 2017a). Subduction of crustal rocks to mantle depth for UHP metamorphism is verified by findings of coesite inclusions in zircon and garnet from gneiss and eclogite (Song et al., 2014; Zhang et al., 2017a). Despite the continental affinity for most metamorphic rocks, some eclogite and associated ultramafic rocks are considered as relics of the oceanic lithosphere that subducted preceding continental subduction (Song et al., 2009, 2014; Zhang et al., 2008, 2009). In contrast to continental eclogite with Neoproterozoic protolith ages, oceanic eclogite is of Cambrian protolith ages (Zhang et al., 2008, 2017b). Nevertheless, both types of eclogite have relatively uniform eclogite facies metamorphic ages of 430–440 Ma (Song et al., 2014; Zhang et al., 2016).

In the Dulan terrane, serpentinite and oceanic eclogite occur along with gneiss and continental eclogite (Zhang et al., 2008; Song et al., 2009, 2014; Fig. 1b). In particular, a cross-section along the Shaliuhe River, consisting of banded kyanite eclogite and enclosed serpentinized harzburgite (left part of Fig. 1c), was described in detail in previous studies (Song et al., 2009; Zhang et al., 2008, 2009). The banded kyanite eclogite, with peak P-T condition of 2.7–3.4 GPa and 610–700 °C, is oceanic eclogite that resembles cumulate oceanic gabbro in both structure and geochemistry (Zhang et al., 2008, 2009). The enclosed serpentinite is conformable with the kyanite eclogite, and no apparent fault is present between them. Instead, gradual transition exists from banded kyanite eclogite to olivine pyroxenite and then to serpentinite. Relict harzburgite olivine and orthopyroxene in the serpentinite display compositions similar to olivine and orthopyroxene in abyssal peridotite, respectively (Song et al., 2009; Zhang et al., 2008). Moreover, presence of highly magnesian secondary olivine in the serpentinite suggests that the serpentinite was involved in subduction and experienced partial dehydration (Song et al., 2009; Zhang et al., 2008). Close association of the kyanite eclogite and enclosed serpentinite indicates that they are probably a coherent unit from seafloor to subduction zone. Therefore, the cross-section was interpreted to represent the lower part of an eclogite-facies metamorphosed ophiolite unit (Song et al., 2009; Zhang et al., 2008).

Besides the serpentinite block mentioned above, most serpentinite bodies in the Dulan terrane are enclosed by continental gneiss. In particular, a small serpentinite block is hosted in granitic gneiss in the Shaliuhe cross-section (right part of Fig. 1c). The granitic gneiss and enclosed continental eclogite record a peak P-T condition of 3.0–3.4 GPa and 655–745 °C (Ren et al., 2016). In addition, the granitic gneiss has similar eclogite-facies metamorphic ages as the nearby oceanic and continental eclogite (Ren et al., 2016). Nevertheless, the gneiss-hosted serpentinite was ignored in previous studies, and its protolith nature and metamorphic evolution are not clear. Moreover, mineral assemblage of the eclogite-hosted serpentinite is not typical of the P-T condition constructed from the oceanic eclogite, and geochemical evolution of the serpentinite is not investigated.

This study investigates in detail the petrology and geochemistry of the large eclogite-hosted serpentinite block and the small gneiss-hosted serpentinite block from the Shaliuhe cross-section (Fig. 1c). Fresh serpentinite in the field has green to dark green color with a heterogeneous appearance due to the uneven distribution of opaque minerals, while weathered serpentinite is severely fragmented with whitish to grey colors (Fig. 2a). In contrast to the concordant contact between the large serpentinite block and the kyanite eclogite (Fig. 2b), the small serpentinite block is in sharp contact with the granitic gneiss (Fig. 2c). Minor rodingite occurs as dykes, lenses, and oval bodies in the serpentinite (Fig. 2d). The serpentinite varies from massive to strongly foliated. Tiny tremolite or late carbonate veinlets can be observed in some serpentinite hand specimens.

## 3. Analytical methods

### 3.1. Whole rock major-trace elements

Whole rock major and trace element contents were analyzed at the State Key Laboratory of Isotope Geochemistry, Guangzhou Institute of Geochemistry (GIG). Major elements were measured by X-ray fluorescence spectrometry on glass disks prepared by fluxing fresh rock powders with $Li_2B_4O_7$. Trace elements were measured by a PerkinElmer Elan 6000 inductively coupled plasma mass spectrometer (ICP-MS) on 2% $HNO_3$ solution after complete dissolution of rock powders following the commonly used $HF/HNO_3/HClO_4$ procedure. Analytical precision and accuracy were better than ±1% for major oxides and better than ±5% for most trace elements, but may deteriorate to ±10% for some trace elements such as Nb, Ta, Hf, etc.

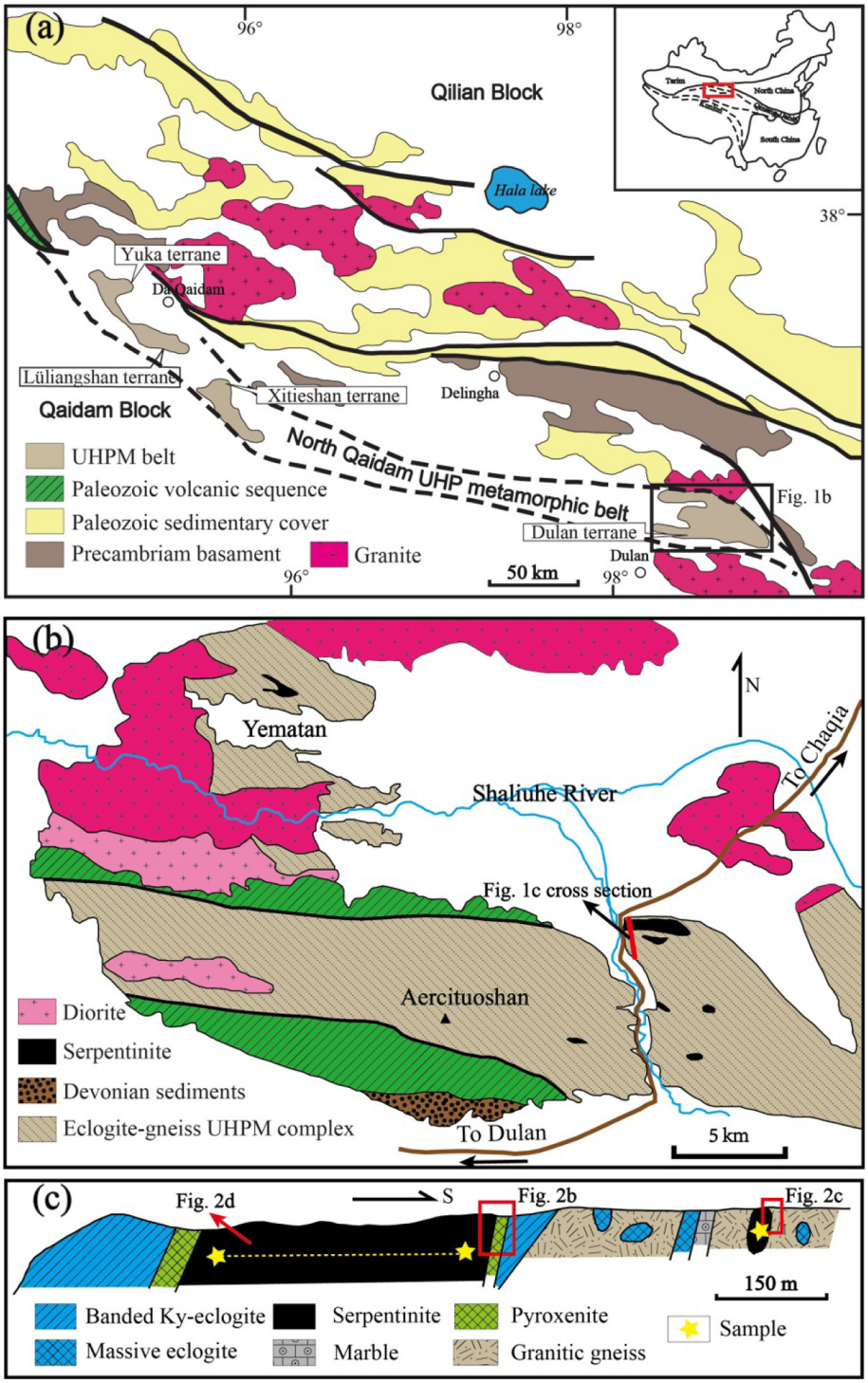


**Fig. 1.** (a) Geological map of the North Qaidam orogen and adjacent areas. (b) Geological map of the Dulan terrane. (c) Serpentinite-bearing cross-section investigated in this study. Samples were collected from both the large and small serpentinite blocks. Modified after Song et al. (2014).

### 3.2. Whole rock O-Sr isotopes

O isotope analyses were accomplished using the laser fluorination technique with a 25 W MIR-10 $CO_2$ laser at the CAS Key Laboratory of Crust–Mantle Materials and Environments, University of Science and Technology of China (Zheng et al., 2002). $O_2$ was produced by reacting ~2.0 mg rock powders with $BrF_5$ upon heating by $CO_2$ laser. Extracted $O_2$ was then directly transferred to a Finnigan MAT-253 mass spectrometer for measurement of O isotope ratios. International standard UWG-2 garnet ($\delta^{18}O = 5.8‰$; Valley et al., 1995) and in-house standard 04BXL07 garnet ($\delta^{18}O = 3.6‰$; Gong et al., 2007) were used as reference standards. The O isotope data are reported using the conventional $\delta^{18}O$ notation relative to VSMOW. Analytical error of $\delta^{18}O$ was better than $\pm$ 0.1%.

Sr isotope analyses were performed using a Neptune plus multi-collector ICP-MS at GIG. Sr was extracted in an ultraclean room with ion-exchange purification by Sr-special resin. Measured $^{87}Sr/^{86}Sr$ ratio was normalized to $^{86}Sr/^{88}Sr = 0.1194$. NIST SRM 987 standard was analyzed repeatedly as monitors and generally yielded results within error of the recommended value. Total analytical blank for Sr was controlled

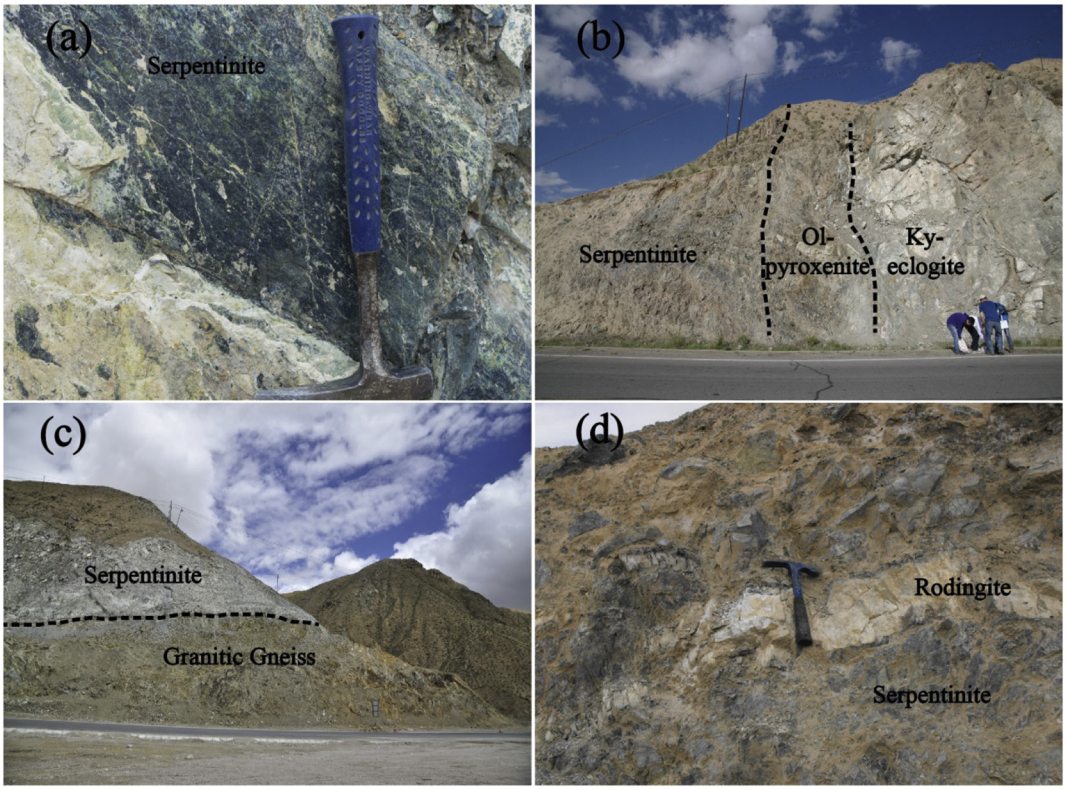


**Fig. 2.** Field occurrence of (a) serpentinite and its relationship with (b) oceanic eclogite, (c) granitic gneiss, and (d) rodingite.

below 200 pg. Parent/daughter ratio of Rb/Sr is calculated from whole rock trace element concentrations determined by ICP-MS. Initial $^{87}Sr/^{86}Sr$ ratio was calculated at t = 440 Ma, which represents the peak eclogite-facies metamorphic age in the North Qaidam (Song et al., 2014; Zhang et al., 2016).

### 3.3. Mineral Raman spectra, major elements, and back-scattered electron image

In-situ micro-Raman spectra of minerals were collected with a WITec Alpha300R confocal Raman microscope at GIG, using a 488 nm laser to avoid fluorescence. Incident power of laser was set at 5–10 mW, and the laser spot size was <1 μm with a 50× objective lens. Spectra accumulation in the wave number range of 100~4000 $cm^{-1}$ were accomplished by five acquisition sequence, with at least 5 seconds per sequence. Identification of Raman peaks and serpentine species was based on the RRUFF database (http://rruff.info) and previous studies (Rinaudo et al., 2003; Rouméjon et al., 2015, 2018).

Major element compositions of rock-forming minerals and back-scattered electron (BSE) images of thin sections were obtained by a JEOL JXA-8100 electron microprobe (EMP) at GIG. Accelerating voltage and beam current were fixed at 15 kV and 20 nA, respectively. Beam radius was commonly set at 5 μm. Counting times were 20s for peak and 10s for background for most elements. Natural silicate standards were used for calibration. Data correction was accomplished using the ZAF procedure. The analytical errors were usually within ± 5%.

## 4. Results

### 4.1. Petrography

Detailed petrography of collected samples is described in Table S1. Serpentine in the samples is mainly lizardite and antigorite. Under the microscope, lizardite is mostly yellow green and antigorite is almost pale to whitish. Moreover, lizardite generally preserves pseudomorph textures while antigorite usually occurs as blades or patches. Lizardite and antigorite are further distinguished by their Raman spectra, with differences in the symmetric $\nu_5$(e) mode of $SiO_4$ tetrahedra, the anti-symmetric Si-$O_b$-Si stretching mode and the OH stretching mode (Fig. S1). Based on the distinction between lizardite and antigorite, the samples can be divided into antigorite serpentinite with antigorite as the sole or dominant serpentine species, and lizardite serpentinite with lizardite as the prevailing serpentine species. The antigorite serpentinite is generally foliated, while the lizardite serpentinite is mostly undeformed. We focus on antigorite serpentinite 09QL36 and lizardite serpentinite 15NQ43 and 17QH241 for petrographic investigation, as they contain secondary olivine and preserve the most complete records of serpentinite evolution. A sequence of mineral paragenesis for these samples is illustrated in Table 1.

The lizardite serpentinite contains numerous relict textures of original peridotite and serpentinization process. Typical mesh texture due to alteration of mantle olivine is widespread, with mesh core occupied by relict mantle olivine or lizardite and mesh rim comprised of lizardite and magnetite (Fig. 3a, b). Magnetite usually crystallizes in the outer mesh rim along previous olivine boundaries, with its trails depicting equilibrium triple junction texture of protolith peridotite (Fig. 3a, b). Highly fragmented relict mantle orthopyroxene is replaced by bastitic lizardite and talc along fracture and periphery (Fig. 3c). Bastite is highlighted by its larger grain size than mesh lizardite, and cleavages of original orthopyroxene occupied by oriented opaque minerals (Fig. 3d). Clinopyroxene exsolution lamellaes are found in some relict orthopyroxene. Instead, no clinopyroxene has been observed in the matrix. Serpentinite with high CaO content is characterized by the presence of a considerable amount of tremolite that is closely associated with lizardite. Meanwhile, abundant lizardite inclusions can be found in some tremolite grains (Fig. 3e). A few serpentinite samples contain tiny veinlets composed mainly of tremolite, lizardite, chlorite, and opaque minerals (Fig. 3f). Chromite occurs as isolated grains, aggregated patches or schlierens, which is usually rimmed by a thin magnetite layer and further coated by chlorite flakes (Fig. 3b, d, g).

There is a gradual transition from the lizardite serpentinite to the antigorite serpentinite. In the lizardite serpentinite, lizardite is initially replaced by antigorite along the periphery, forming interconnected antigorite networks (Fig. 4a). These networks can occasionally be traced back to antigorite veinlets with irregular boundaries that cut mesh or bastitic lizardite (Fig. 4b). With increasing degrees of antigorite growth, antigorite starts to accumulate as patches. In lizardite-bearing antigorite serpentinite, only minor serpentinization domains are scattered in the antigorite-dominated matrix (Fig. 4c). In antigorite serpentinite without lizardite, traces of olivine and orthopyroxene pseudomorphs can still be identified, with the outline of olivine highlighted by magnetite trails and the site of orthopyroxene occupied by relatively coarse-grained antigorite. The textures of chromite and chlorite in the antigorite serpentinite are mostly similar to those in the lizardite serpentinite (Fig. 3h). However, some chromite grains without chlorite coatings are associated with antigorite veinlet (Fig. 4b), and isolated chlorite flake is occasionally included by patchy antigorite (Fig. 3h).

Secondary olivine, with its texture differing greatly from relict mantle olivine, is observed in antigorite serpentinite 09QL36 and lizardite serpentinite 15NQ43 and 17QH241 (Fig. 4d, e, f, g, h). Nonetheless, only rare secondary olivine restricted to specific domains has been observed in 15NQ43 and 17QH241. In 09QL36, small clear secondary olivine grains are crosscut or clamped by antigorite blades (Fig. 4d). In 15NQ43, clusters of secondary olivine occupy the sites of original mesh lizardite (Fig. 4e, f). The secondary olivine varies greatly in grain size and is highly anhedral, in contrast to generally oval relict olivine in mesh core (Fig. 4e, f). The secondary olivine seems dirty in contrast to clear relict olivine and secondary olivine in 09QL36, which is due to its association with opaque minerals (Fig. 4e, g). Serpentine surrounding the secondary olivine is either antigorite or transitional serpentine (Figs. 4e and S1). In 17QH241, numerous minute grains of secondary olivine appear in several sites of former bastite (Fig. 4g, h). The olivine grains are aligned in parallel to oriented opaque minerals occupying cleavages of previous orthopyroxene (Fig. 4g). Lizardite and rare talc can be detected in the pseudomorph (Fig. S1). Serpentine neighboring secondary olivine is mostly transitional between lizardite and antigorite.

### 4.2. Whole rock major-trace elements

Fifteen fresh hand specimens free of obvious tremolite and carbonate veinlets were selected for analysis of bulk rock major and trace elements, and the results are reported in Table 2 and illustrated in Fig. 5, 6. The lizardite serpentinite and antigorite serpentinite have overlapping major element compositions, which are characterized by high $SiO_2$, MgO, and FeO, and low $Al_2O_3$ and CaO (Fig. 5a, b, c and d). The resultant $Al_2O_3/SiO_2$ and $MgO/SiO_2$ ratios are 0.017–0.039 and 0.91–1.00, respectively (Fig. 5e). The samples have high loss on ignition (LOI) from 11.11% to 13.61%, indicating high degrees of serpentinization.

All samples have low concentrations of rare earth elements (REE) and high field strength elements (HFSE) with respect to the depleted mantle (Fig. 6). They display U-shaped chondrite normalized REE patterns (Fig. 6a), with $(La/Sm)_N$ and $(Gd/Yb)_N$ ratios of 1.3–3.0 and 0.3–1.1, respectively. In the primitive mantle normalized spider-diagram (Fig. 6b), the serpentinite is characterized by strong enrichments in Cs, U, and Pb. Instead, other large ion lithophile elements are not significantly spiked. The lizardite serpentinite and antigorite serpentinite have comparable concentrations of immobile elements. However, the lizardite serpentinite has higher U and lower Cs, Rb, and Ba than the antigorite serpentinite.

### 4.3. Whole rock O-Sr isotopes

O and Sr isotopic compositions of selective samples (including host gneiss) are presented in Table 3 and Fig. 7. The antigorite serpentinite has relatively constant $\delta^{18}O$ of 4.0‰–4.5‰, whereas three lizardite serpentinite samples have much lower $\delta^{18}O$ of 2.7‰, 2.4‰, and 0.6‰. Two gneiss samples have high $\delta^{18}O$ of 9.0‰ and 10.4‰. The antigorite serpentinite has high initial $^{87}Sr/^{86}Sr$ of 0.711317–0.713996, while the lizardite serpentinite has lower initial $^{87}Sr/^{86}Sr$ of 0.708319–0.709308. Two gneiss samples have even lower initial $^{87}Sr/^{86}Sr$ of 0.706340 and 0.707109.

**Table 1**
Evolution of mineral assemblages in antigorite serpentinite 09QL36 and lizardite serpentinite 15NQ43 and 17QH241.

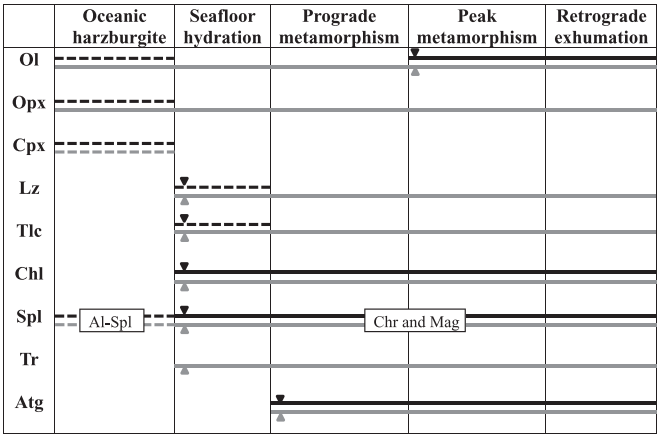


Notes: Black line is for antigorite serpentinite 09QL36, grey line is for lizardite serpentinite 15NQ43/17QH241. Solid and dashed lines represent minerals that are and are not present in thin section, respectively. Mantle olivine and orthopyroxene, lizardite, talc, chlorite, chromite/magnetite and tremolite are metastable in subducted serpentinite. The arrow dictates first appearance of a mineral except relics from mantle harzburgite.

### 4.4. Mineral major elements

Complete dataset reporting representative mineral major element compositions of the three target samples (09QL36, 15NQ43, and 17QH241) is listed in Table S2. Relict olivine in 15NQ43 and 17QH241 has high Mg# (=Mg/(Mg+Fe)) of ~0.90, with minor amounts of NiO (0.32%–0.38%) and MnO (0.12%–0.19%). In contrast, secondary olivine shows large variations in composition. Secondary olivine in 09QL36 has higher Mg# (0.93–0.96) than relict olivine, whereas secondary olivine in 15NQ43 and 17QH241 has lower Mg# of 0.76–0.85 and 0.84–0.87, respectively (Fig. 8a, b). Nonetheless, secondary olivine from all samples is characterized by higher MnO (0.25%–1.33%) and lower NiO (0.04%–0.37%) than relict olivine (Fig. 8a, b). Relict orthopyroxene in 15NQ43 and 17QH241 is characterized by Mg# of ~0.90, moderate amounts of $Al_2O_3$ (2.55%–3.55%) and minor amounts of $Cr_2O_3$ (0.41%–0.66%) (Fig. 8c, d).

Serpentine has a wide range of composition (Fig. 9), primarily depending on polymorph type and texture. Normalizing serpentine composition to seven O ions, lizardite is typified by Si atoms per formula unit (apfu) generally <2.0 (Fig. 9a). Lizardite has Mg# (0.85–0.92) straddling between those of antigorite and ferroan metamorphic olivine (Fig. 9b). Moreover, lizardite inherits the composition of its parent mineral, with bastitic lizardite containing higher $Al_2O_3$ and $Cr_2O_3$ and lower NiO than mesh lizardite (Fig. 9c, d). Matrix lizardite without recognizable precursor mineral is either mesh-like or bastite-like in composition. Lizardite within tremolite veinlet is similar to mesh lizardite. There is large compositional contrast between antigorite and lizardite. Antigorite is enriched in silica with Si apfu usually >2.0 (Fig. 9a). Moreover, antigorite has elevated Mg# that is higher than both relict olivine and lizardite (Fig. 9b). Nonetheless, antigorite has lower FeO and MnO than lizardite (Fig. 9b, c). Transitional serpentine neighboring secondary olivine in 15NQ43 and 17QH241 has composition that approaches antigorite (Fig. 9).

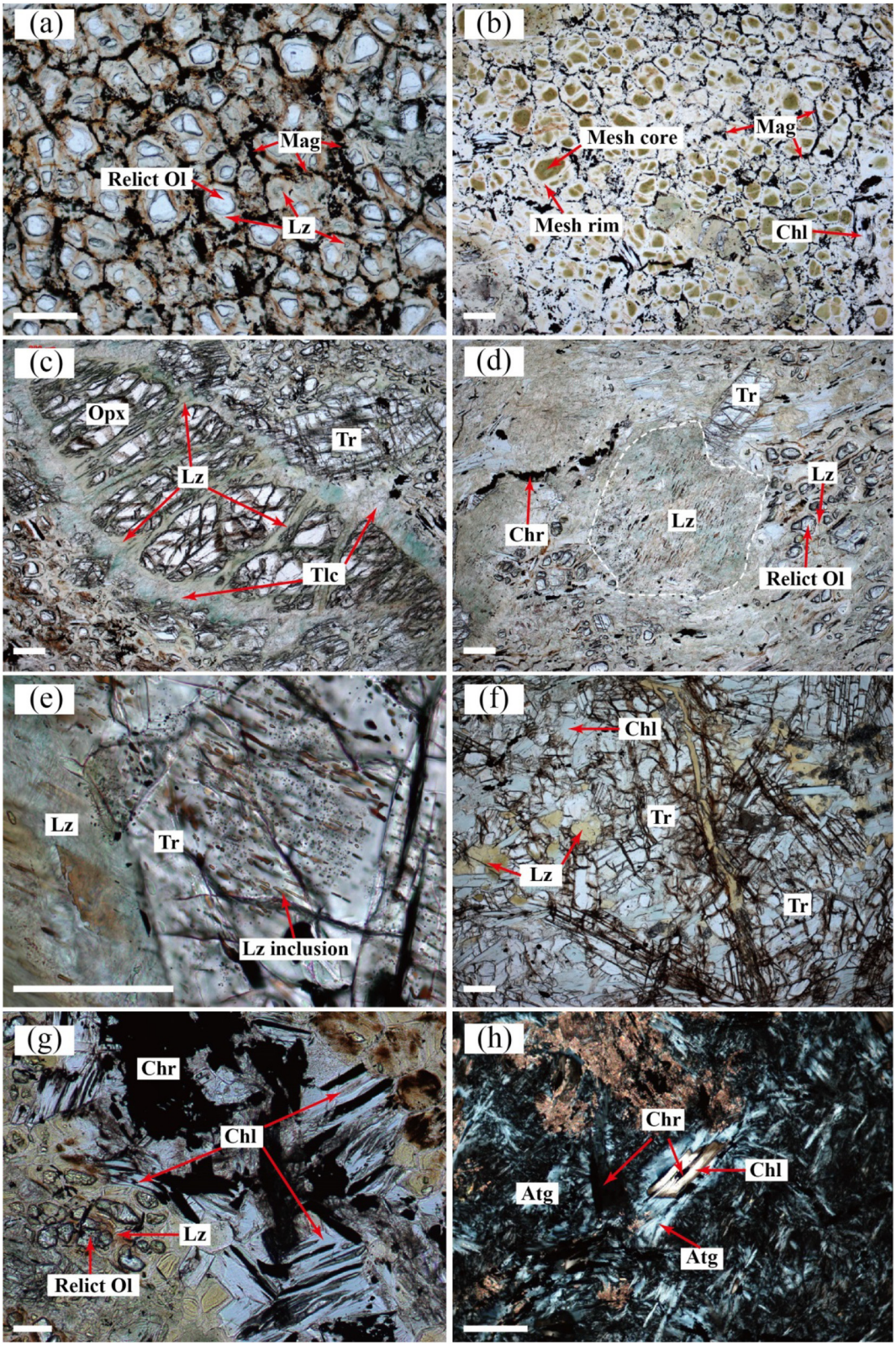


**Fig. 3.** Microphotographs showing textures related to serpentinization in the serpentinite. (a) Replacement of mantle olivine by mesh lizardite and magnetite in 15NQ45. (b) Mesh lizardite with core-rim texture in 15NQ45. Magnetite occurs along the boundary of previous olivine in (a) and (b), depicting equilibrium triple junction texture of protolith peridotite. (c) Replacement of mantle orthopyroxene by bastitic lizardite and talc in 15NQ44. (d) Co-existence of mesh and bastitic lizardite (circled by dotted line) in 15NQ43. Cleavages of previous orthopyroxene are highlighted by oriented opaque minerals in bastite. (e) Tremolite with numerous oriented tiny lizardite inclusions in 15NQ43. (f) Veinlet composed of tremolite, lizardite, and chlorite in 15NQ43. (g) Chromite aggregates coated by chlorite flakes in 15NQ44. (h) Chlorite including a chromite core is surrounded by patchy antigorite in 09QL36. The scale bar is 200 μm. Abbreviations of mineral names in this paper are after Whitney and Evans (2010).

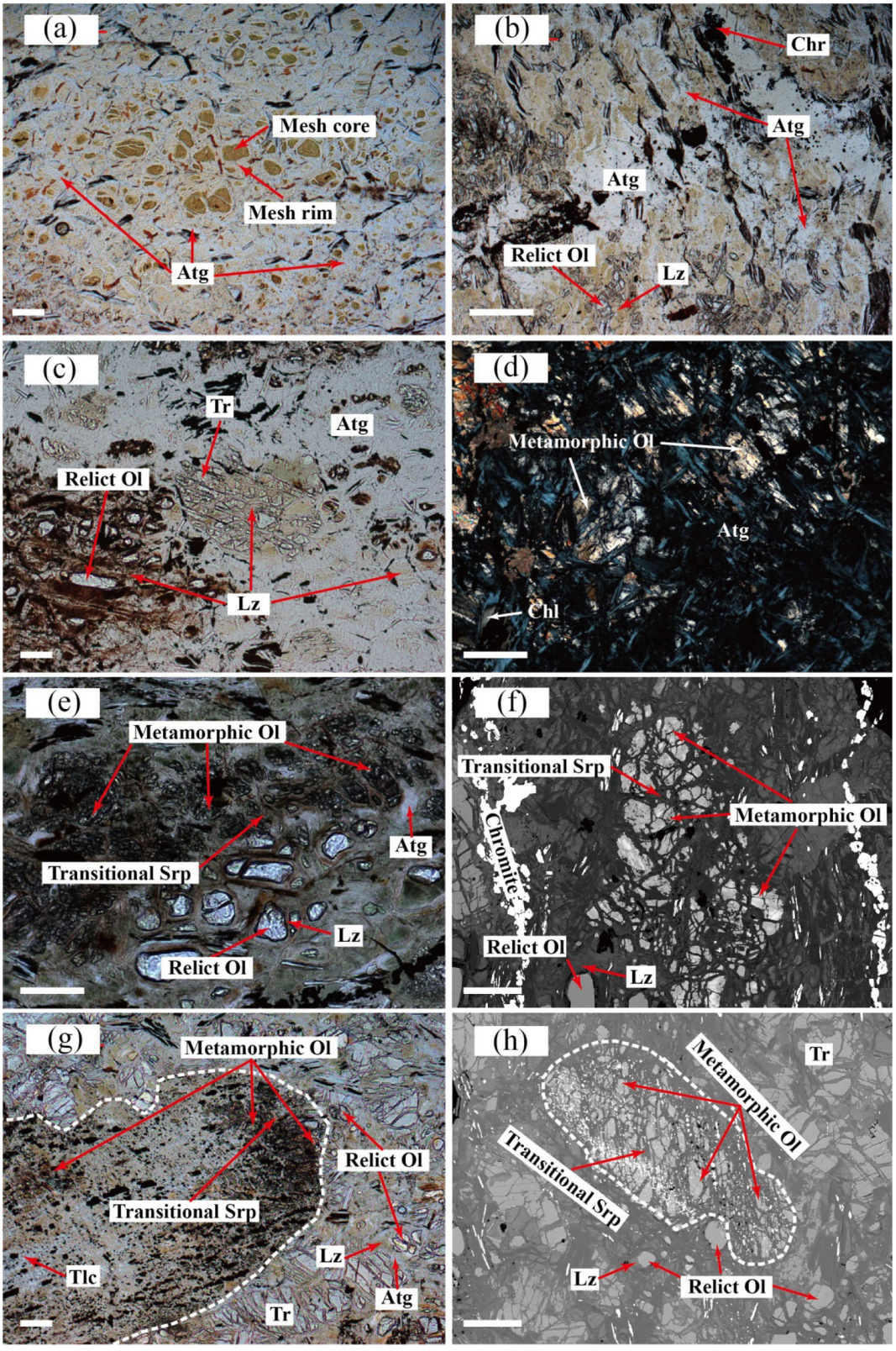


**Fig. 4.** Microphotographs showing textures related to subduction zone metamorphism in the serpentinite. (a) Interconnected antigorite networks replacing mesh lizardite along peripheries in 17QH241. (b) Antigorite veinlet cutting and penetrating into lizardite in 17QH241. (c) Domains of relict mesh lizardite, mantle olivine and tremolite surrounded by antigorite-dominated matrix in 17QH224. In (a–c), lizardite and antigorite are yellow green and pale to whitish, respectively. (d) Secondary magnesian olivine interspaced with antigorite blades in 09QL36. (e) Secondary ferroan olivine occupying the site of original mesh lizardite in 15NQ43. Serpentine neighboring secondary olivine is either transitional serpentine or antigorite. (f) BSE image of the same domain as (e) with a 90° rotation. (g) Orthopyroxene pseudomorph (circled by dotted line) now composed of secondary ferroan olivine, serpentine, talc and opaque minerals in 17QH241. (h) BSE image of an orthopyroxene pseudomorph (circled by dotted line) similar to (g), but with negligible talc and more secondary olivine. Stark contrast exists between secondary and relict olivine in (e–g). The scale bar denotes 200 μm.

**Table 2**
Whole-rock element concentrations of the North Qaidam serpentinite.

| Sample No. | Antigorite serpentinite | | | | | | | | Lizardite serpentinite | | | | | | |
|---|---|---|---|---|---|---|---|---|---|---|---|---|---|---|---|
| | 09QL36 | 09QL37 | 09QL44 | 15NQ 33 | 15NQ 39 | 15NQ 40 | 17QH220 | 17QH221 | 17QH224 | 15NQ43 | 15NQ 44 | 15NQ 45 | 17QH241 | 17QH244 | 17QH249 |
| Major oxides (%) | | | | | | | | | | | | | | | |
| $SiO_2$ | 38.05 | 40.26 | 39.58 | 40.50 | 41.11 | 39.99 | 39.61 | 39.43 | 39.96 | 41.26 | 40.27 | 39.18 | 40.45 | 39.26 | 39.39 |
| $TiO_2$ | 0.01 | 0.03 | 0.01 | 0.02 | 0.02 | 0.02 | 0.01 | 0.03 | 0.02 | 0.01 | 0.02 | 0.03 | <0.01 | 0.02 | 0.03 |
| $Al_2O_3$ | 1.22 | 1.45 | 1.10 | 1.13 | 1.35 | 1.11 | 0.66 | 0.98 | 0.88 | 1.42 | 1.56 | 1.02 | 1.42 | 1.07 | 1.14 |
| FeO | 6.66 | 7.10 | 7.30 | 8.11 | 7.62 | 7.75 | 7.54 | 7.42 | 7.33 | 7.12 | 7.27 | 7.92 | 6.95 | 6.98 | 7.17 |
| MnO | 0.08 | 0.06 | 0.08 | 0.08 | 0.07 | 0.08 | 0.07 | 0.09 | 0.12 | 0.11 | 0.12 | 0.13 | 0.10 | 0.11 | 0.12 |
| MgO | 36.45 | 38.57 | 38.44 | 37.08 | 37.66 | 37.67 | 38.60 | 38.48 | 38.47 | 37.36 | 36.78 | 37.90 | 37.74 | 39.27 | 38.48 |
| CaO | 2.64 | 0.21 | 0.44 | 0.26 | 0.07 | 0.03 | 0.67 | 0.66 | 0.17 | 1.65 | 1.37 | 0.69 | 1.10 | 0.13 | 0.35 |
| $Cr_2O_3$ | 0.38 | 0.40 | 0.35 | 0.39 | 0.37 | 0.39 | 0.33 | 0.55 | 0.41 | 0.35 | 0.35 | 0.44 | 0.36 | 0.35 | 0.40 |
| LOI | 13.61 | 12.25 | 12.15 | 11.82 | 11.75 | 12.26 | 12.70 | 12.64 | 12.75 | 11.11 | 11.96 | 12.48 | 11.75 | 13.19 | 13.27 |
| Total | 99.10 | 100.35 | 99.45 | 99.40 | 100.03 | 99.31 | 100.18 | 100.28 | 100.12 | 100.39 | 99.71 | 99.80 | 99.88 | 100.39 | 100.37 |
| Mg# | 0.907 | 0.906 | 0.904 | 0.891 | 0.898 | 0.896 | 0.901 | 0.902 | 0.903 | 0.903 | 0.900 | 0.895 | 0.906 | 0.909 | 0.905 |
| Trace elements (ppm) | | | | | | | | | | | | | | | |
| Li | 0.26 | 0.11 | 0.11 | 0.17 | 0.15 | 0.20 | 0.56 | 0.82 | 0.80 | 2.56 | 3.21 | 1.28 | 1.76 | 0.81 | 0.66 |
| Be | 0.064 | 0.016 | 0.012 | 0.010 | 0.016 | 0.006 | 0.010 | 0.009 | 0.011 | 0.011 | 0.013 | 0.005 | 0.009 | 0.006 | 0.009 |
| Sc | 10.0 | 9.5 | 8.3 | 9.2 | 9.3 | 9.3 | 7.5 | 9.1 | 8.8 | 10.8 | 9.6 | 10.2 | 10.7 | 8.8 | 10.3 |
| V | 39.0 | 31.7 | 38.3 | 35.6 | 41.1 | 27.8 | 26.5 | 35.5 | 31.5 | 43.5 | 41.0 | 36.4 | 51.8 | 32.8 | 38.9 |
| Co | 89.5 | 85.9 | 87.9 | 88.1 | 81.8 | 98.7 | 84.1 | 102.8 | 91.5 | 87.4 | 86.6 | 94.9 | 87.6 | 88.5 | 88.0 |
| Ni | 1799 | 1781 | 1846 | 1909 | 1806 | 1675 | 1826 | 1893 | 1877 | 1711 | 1771 | 1817 | 1783 | 1834 | 1706 |
| Cu | 1.66 | 30.4 | 2.17 | 1.19 | 1.97 | 0.98 | 26.7 | 28.3 | 26.9 | 27.8 | 8.93 | 27.4 | 5.05 | 0.78 | 11.0 |
| Zn | 37.5 | 23.5 | 38.7 | 30.4 | 34.7 | 31.5 | 32.9 | 41.7 | 41.9 | 33.5 | 37.4 | 42.0 | 34.6 | 39.2 | 35.1 |
| Rb | 0.113 | 0.079 | 0.081 | 0.083 | 0.094 | 0.059 | 0.080 | 0.080 | 0.127 | 0.231 | 0.430 | 0.204 | 0.177 | 0.103 | 0.073 |
| Sr | 17.9 | 6.6 | 30.5 | 5.4 | 2.6 | 2.1 | 98.5 | 9.0 | 2.9 | 6.5 | 5.5 | 4.6 | 3.9 | 1.6 | 2.2 |
| Y | 0.533 | 0.411 | 0.359 | 0.394 | 0.379 | 0.250 | 0.275 | 0.408 | 0.344 | 0.599 | 0.461 | 0.434 | 0.536 | 0.461 | 0.476 |
| Zr | 1.15 | 0.959 | 0.797 | 0.406 | 0.267 | 0.372 | 0.521 | 0.617 | 0.749 | 0.504 | 0.237 | 0.383 | 0.475 | 0.271 | 0.408 |
| Nb | 0.089 | 0.074 | 0.045 | 0.046 | 0.030 | 0.043 | 0.062 | 0.102 | 0.059 | 0.089 | 0.061 | 0.055 | 0.063 | 0.052 | 0.067 |
| Cs | 0.024 | 0.014 | 0.015 | 0.028 | 0.034 | 0.010 | 0.016 | 0.041 | 0.091 | 0.205 | 0.260 | 0.091 | 0.173 | 0.068 | 0.048 |
| Ba | 0.678 | 0.449 | 1.05 | 0.681 | 0.473 | 0.339 | 1.29 | 0.857 | 0.910 | 1.52 | 3.12 | 1.95 | 0.886 | 0.815 | 0.351 |
| La | 0.076 | 0.134 | 0.080 | 0.116 | 0.099 | 0.067 | 0.130 | 0.165 | 0.140 | 0.149 | 0.182 | 0.123 | 0.228 | 0.189 | 0.119 |
| Ce | 0.197 | 0.343 | 0.176 | 0.236 | 0.213 | 0.138 | 0.227 | 0.389 | 0.247 | 0.364 | 0.462 | 0.264 | 0.497 | 0.412 | 0.257 |
| Pr | 0.031 | 0.053 | 0.026 | 0.032 | 0.029 | 0.018 | 0.030 | 0.058 | 0.031 | 0.058 | 0.071 | 0.039 | 0.067 | 0.056 | 0.037 |
| Nd | 0.145 | 0.260 | 0.111 | 0.132 | 0.110 | 0.072 | 0.128 | 0.258 | 0.129 | 0.276 | 0.302 | 0.177 | 0.272 | 0.216 | 0.171 |
| Sm | 0.033 | 0.065 | 0.025 | 0.028 | 0.023 | 0.014 | 0.032 | 0.061 | 0.035 | 0.062 | 0.054 | 0.045 | 0.053 | 0.044 | 0.045 |
| Eu | 0.008 | 0.008 | 0.012 | 0.012 | 0.011 | 0.010 | 0.015 | 0.021 | 0.015 | 0.017 | 0.019 | 0.015 | 0.018 | 0.014 | 0.015 |
| Gd | 0.036 | 0.067 | 0.027 | 0.035 | 0.024 | 0.018 | 0.035 | 0.059 | 0.046 | 0.064 | 0.050 | 0.047 | 0.055 | 0.046 | 0.050 |
| Tb | 0.008 | 0.012 | 0.006 | 0.007 | 0.006 | 0.004 | 0.007 | 0.011 | 0.009 | 0.013 | 0.009 | 0.010 | 0.010 | 0.010 | 0.010 |
| Dy | 0.065 | 0.070 | 0.047 | 0.054 | 0.051 | 0.031 | 0.043 | 0.073 | 0.055 | 0.089 | 0.069 | 0.066 | 0.078 | 0.065 | 0.075 |
| Ho | 0.018 | 0.015 | 0.012 | 0.014 | 0.013 | 0.008 | 0.010 | 0.016 | 0.012 | 0.022 | 0.017 | 0.016 | 0.020 | 0.017 | 0.017 |
| Er | 0.055 | 0.041 | 0.039 | 0.046 | 0.044 | 0.030 | 0.027 | 0.043 | 0.032 | 0.066 | 0.056 | 0.047 | 0.061 | 0.052 | 0.051 |
| Tm | 0.010 | 0.008 | 0.007 | 0.009 | 0.009 | 0.005 | 0.005 | 0.007 | 0.005 | 0.012 | 0.009 | 0.008 | 0.011 | 0.009 | 0.009 |
| Yb | 0.072 | 0.058 | 0.051 | 0.062 | 0.062 | 0.046 | 0.035 | 0.051 | 0.035 | 0.085 | 0.070 | 0.060 | 0.075 | 0.064 | 0.064 |
| Lu | 0.012 | 0.010 | 0.009 | 0.011 | 0.011 | 0.009 | 0.006 | 0.009 | 0.006 | 0.015 | 0.012 | 0.012 | 0.013 | 0.011 | 0.010 |
| Hf | 0.042 | 0.042 | 0.034 | 0.023 | 0.015 | 0.019 | 0.024 | 0.031 | 0.036 | 0.028 | 0.017 | 0.026 | 0.024 | 0.018 | 0.026 |
| Ta | 0.011 | 0.006 | 0.004 | 0.004 | 0.003 | 0.004 | 0.004 | 0.005 | 0.003 | 0.007 | 0.002 | 0.004 | 0.004 | 0.003 | 0.004 |
| Pb | 0.364 | 0.379 | 0.303 | 0.517 | 0.478 | 0.300 | 2.87 | 0.204 | 0.189 | 0.292 | 0.386 | 0.224 | 0.180 | 0.222 | 0.142 |
| Th | 0.015 | 0.039 | 0.011 | 0.015 | 0.009 | 0.007 | 0.018 | 0.070 | 0.027 | 0.095 | 0.045 | 0.012 | 0.037 | 0.046 | 0.014 |
| U | 0.103 | 0.011 | 0.438 | 6.73 | 0.356 | 0.350 | 3.83 | 4.52 | 1.71 | 0.011 | 0.018 | 0.010 | 0.011 | 0.037 | 0.004 |

Chlorite corresponds to clinochlore with constant Mg# of 0.93–0.95. Chlorite usually contains considerable amounts of $Cr_2O_3$ (1.04%–2.68%), and grains coating chromite aggregate can have higher $Cr_2O_3$. Tremolite and talc are near endmembers with minor iron and Tschermak substitutions. Magnetite usually contains detectable amounts of transition metals other than Fe. Chromite is ferritchromite that contains considerable amounts of MgO, MnO, and $Al_2O_3$.

### 4.5. Phase diagram modelling

A P-T pseudosection was calculated by Perple_X (Connolly, 2005) for antigorite serpentinite 09QL36, as it contains well-equilibrated olivine and antigorite with only minor mantle relics. The calculation was accomplished in the FeO-MgO-$Al_2O_3$-$SiO_2$-$H_2O$ system, with minor components neglected for simplicity. CaO is ignored in the calculation, as it is introduced by late carbonate. Thermodynamic database of Holland and Powell (1998, updated in 2002) is adopted. Mineral solution models employed are as follows: olivine and garnet from Holland and Powell (1998), orthopyroxene from Holland and Powell (1996), chlorite from Holland et al. (1998), antigorite from Padrón-Navarta et al. (2013), talc and brucite as pure phases. Fe stored in chromite is removed from bulk rock composition, assuming that Cr is mostly stored in chromite. Five percent (mass proportion) magnetite is also subtracted from the bulk rock composition by converting $Fe_2O_3$ to FeO. Chlorite is not excluded from the bulk rock composition, and the pseudosection calculated without including chlorite generally yields a similar topology as that including chlorite. The effective bulk composition obtained is as follows: $SiO_2$-49.21%, $Al_2O_3$-1.58%, FeO-2.06%, and MgO-47.15%. The corresponding bulk rock Mg# of 0.976 is consistent with dominating antigorite with Mg# of ~0.98 and subordinate olivine with Mg# of 0.93–0.96 in the sample.

As shown in the calculated pseudosection of Fig. 10, the assemblage of antigorite and olivine is stable within the temperature range of 500–600 °C. This temperature range is much lower than the peak temperature constructed from nearby eclogite and gneiss. The olivine Mg# in the stability field of antigorite-olivine is slightly lower than the measured value, which is instead similar to olivine Mg# in the stability field of antigorite-olivine-orthopyroxene. Nevertheless, secondary orthopyroxene has not been identified in the samples. Chlorite is not a stable phase coexisting with antigorite and olivine, due to the low

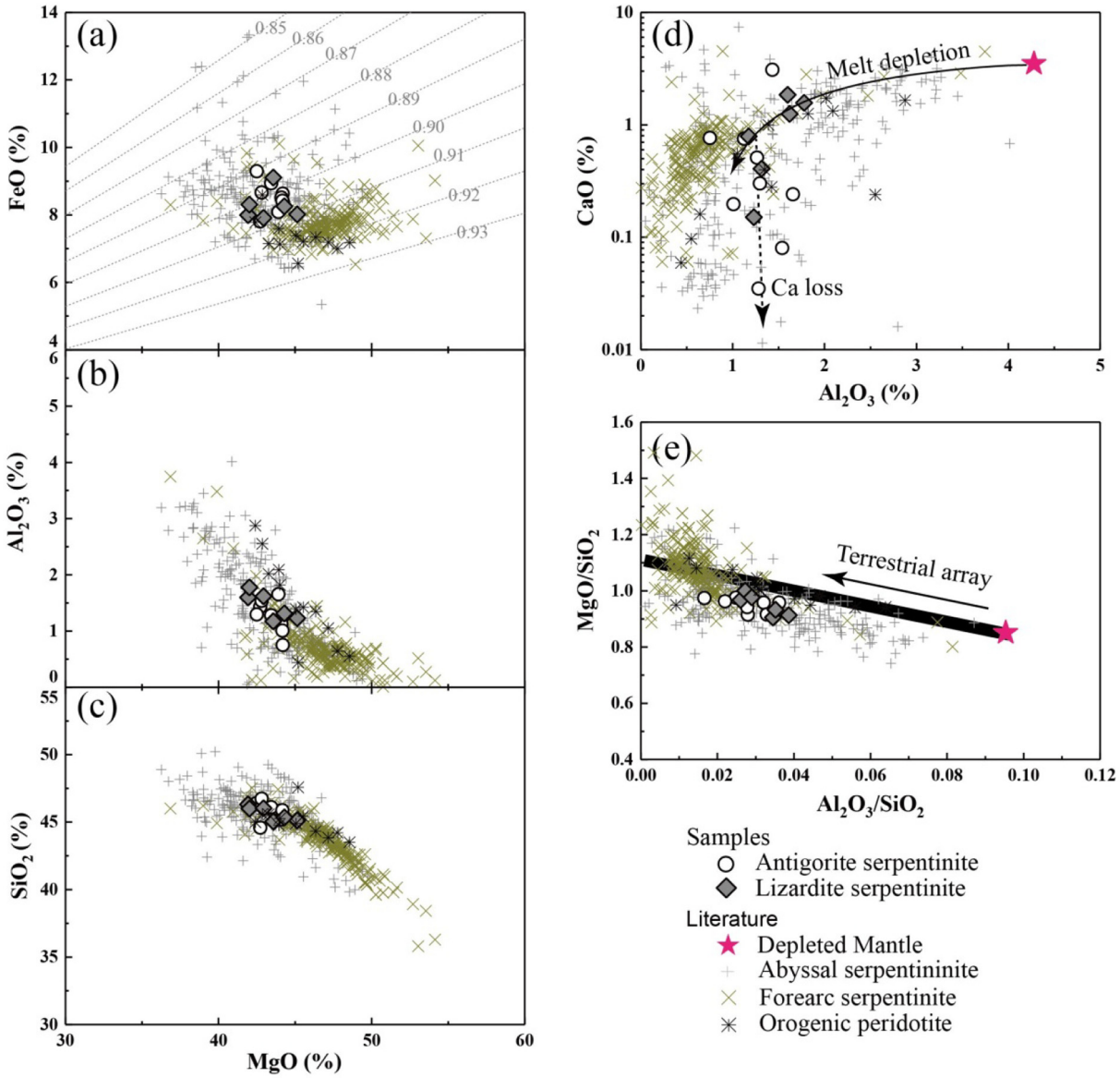


**Fig. 5.** (a) FeO versus MgO, (b) $Al_2O_3$ versus MgO, (c) $SiO_2$ versus MgO, (d) CaO versus $Al_2O_3$, and (e) $MgO/SiO_2$ versus $Al_2O_3/SiO_2$ diagrams for the serpentinite. The data for the depleted mantle are from Salters and Stracke (2004), abyssal serpentinite and forearc serpentinite are from Peters et al. (2017), and Lüliangshan orogenic peridotite are from Song et al. (2007). The dotted lines in (a) labelled with numbers represent Mg# of serpentinite. The melt depletion trend in (d) is after Niu (2004), and the terrestrial array in (e) is after Jagoutz et al. (1979) and Hart and Zindler (1986).

bulk rock $Al_2O_3$. Breakdown of chlorite into patchy antigorite in 09QL36 also illustrates that chlorite and antigorite are not in equilibrium (Fig. 3g).

## 5. Discussion

### 5.1. Protolith nature of the serpentinite

Serpentinite in HP-UHP metamorphic belts can have complicated origins (Deschamps et al., 2013; Evans et al., 2013). On the one hand, it can represent cumulate of mafic melt or residual mantle peridotite from diverse settings. On the other hand, serpentinization of original peridotite may occur on seafloor, in forearc plane above subducting slab or within deep subduction channel. Moreover, the North Qaidam experienced tectonic evolution from oceanic subduction to continental collision (Song et al., 2014; Zhang et al., 2008, 2016, 2017b), with possible derivation of serpentinite from either oceanic or continental settings. Nonetheless, petrography of the Shaliuhe serpentinite reveals that initial hydration preceded gradual subduction zone metamorphism, indicating primary serpentinization at shallow depth before subduction zone overprint.

Overlapping compositions of the lizardite serpentinite and antigorite serpentinite (Fig. 5, 6) indicate that they should have similar protolith nature. Lizardite dominated by mesh texture with subordinate bastite texture in the lizardite serpentinite reveals that the serpentinite was originally harzburgite. Relict clinopyroxene is not observed in the serpentinite matrix. Nevertheless, the presence of considerable tremolite in some samples implies that clinopyroxene was a minor constituting mineral in primordial harzburgite (Section 5.2.1). Moreover, the characteristics of chromite and associated chlorite indicate their production by alteration of Al-rich spinel (Section 5.2.1). Therefore, the Shaliuhe serpentinite was originally refractory clinopyroxene-bearing spinel harzburgite. The depleted nature of the serpentinite is consistent with its high Mg# (0.89–0.91) and low $Al_2O_3$ (Fig. 5a, b). The samples plot at the refractory end of the terrestrial melting array in the diagram of $Al_2O_3/SiO_2$ versus $MgO/SiO_2$ (Fig. 5e), demonstrating considerable

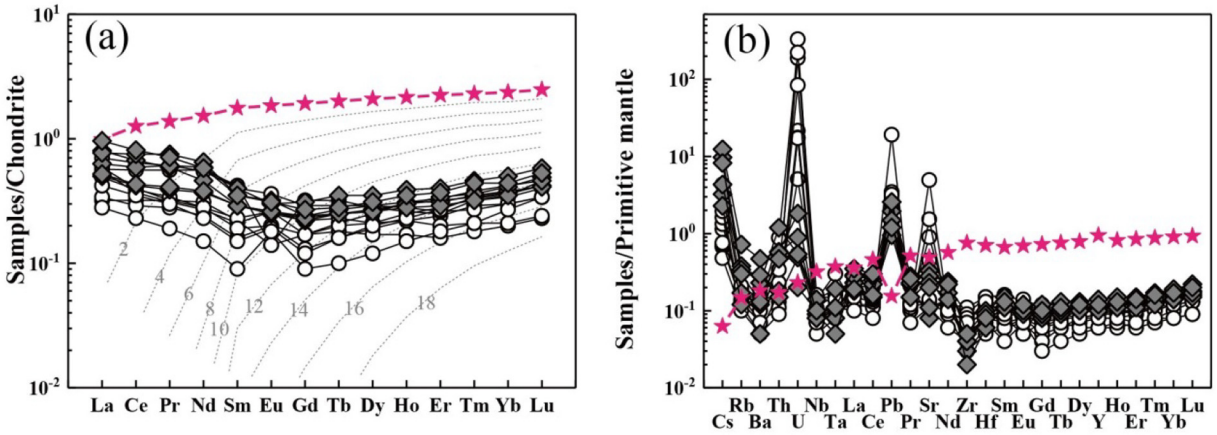


**Fig. 6.** (a) Chondrite-normalized REE patterns for the serpentinite. The chondrite REE contents are from Sun and McDonough (1989), and the depleted mantle REE contents are from Salters and Stracke (2004). The dotted line represent modelled melting residue of the depleted mantle with the number representing melting degrees, where the melting model is after Warren (2016). (b) Primitive mantle-normalized spider-diagram for the serpentinite. Element contents of the primitive mantle are from McDonough and Sun (1995). Symbols are as in Fig. 5.

degrees of melt extraction from protolith harzburgite. Melting model by systematics of heavy REE shows that the serpentinite corresponds to residue of the depleted mantle after 12%–16% degrees of partial melting (Fig. 6a). Existence of clinopyroxene in protolith harzburgite is thus also supported by the melting model, as clinopyroxene is usually eliminated at melting degrees of ~20% in fertile mantle peridotite (Walter, 2003). Refractory mineralogy and geochemistry of the Shaliuhe serpentinite imply that the serpentinite was probably abyssal serpentinite or mantle wedge serpentinite. Further distinction is needed by comparing the serpentinite and its possible protolith.

Petrological and geochemical studies have revealed that abyssal serpentinite is on average less depleted than oceanic forearc serpentinite, in spite of significant overlap between them (Deschamps et al., 2013). Oceanic forearc serpentinite has overall slightly higher MgO, but lower FeO, $Al_2O_3$, and $SiO_2$ than abyssal serpentinite (Fig. 5a, b, c). Consequently, oceanic forearc serpentinite has overall higher Mg# and MgO/$SiO_2$, but lower $Al_2O_3/SiO_2$ than abyssal serpentinite (Fig. 5a, e). The distinction is more profound in mineral compositions of original peridotite (Fig. 8). Olivine and orthopyroxene in oceanic forearc mantle peridotite have higher Mg# than olivine and orthopyroxene in abyssal peridotite, and orthopyroxene in abyssal peridotite has higher $Al_2O_3$ and $Cr_2O_3$ than orthopyroxene in oceanic forearc mantle peridotite (Fig. 8). However, forearc serpentinite may also originate from subcontinental mantle in the North Qaidam orogen. Lüliangshan orogenic peridotite from the west segment of the orogen, which is incorporated into subduction channel for UHP metamorphism, is representative of such subcontinental mantle wedge peridotite (Chen et al., 2017; Song et al., 2014; Xiong et al., 2015). It has been shown that olivine-rich Lüliangshan peridotite is highly refractory Archean mantle residue (Shi et al., 2010; Xiong et al., 2015) with high whole rock and mineral Mg# that is comparable to present oceanic forearc peridotite (Fig. 5, 8).

The Shaliuhe serpentinite is similar to abyssal serpentinite in bulk rock and relict mineral compositions, and it differs from oceanic and continental forearc mantle peridotite (Fig. 5, 8). Therefore, the Shaliuhe serpentinite was originally abyssal serpentinite that underwent hydration on seafloor in the presence of seawater, which is also verified by O isotopes. Abyssal serpentinite can have $\delta^{18}O$ that is lower or higher than the normal mantle, depending primarily on serpentinization temperatures (Kyser et al., 1999; Saccocia et al., 2009; Wenner and Taylor, 1973, 1974). In contrast, forearc serpentinite generally has $\delta^{18}O$ higher than the normal mantle, because the hydrating fluids are mainly derived from subducting sediments (Alt and Shanks, 2006). The Shaliuhe antigorite serpentinite has uniform $\delta^{18}O$ of 4.0%–4.5‰, which implies high temperature seawater alteration of protolith harzburgite. In addition, $\delta^{18}O$ of the antigorite serpentinite is similar to $\delta^{18}O$ of nearby oceanic eclogite (Fig. 7a), implying coherent high temperature hydrothermal alteration of the serpentinite and eclogite. This also demonstrates that $\delta^{18}O$ of the antigorite serpentinite is a remnant of oceanic imprint that was not significantly modified during late stages. In contrast, the lizardite serpentinite has much lower $\delta^{18}O$, with $\delta^{18}O$ of one sample as low as 0.6‰. It has been shown that lizardite is easily subject to exchanging O with meteoric water, and antigorite is generally resistant to weathering (Kyser et al., 1999; Wenner and Taylor, 1973, 1974). Therefore, low $\delta^{18}O$ of the lizardite serpentinite is probably due to O isotope resetting during infiltration of meteoric water at the Earth's surface after exhumation. Nevertheless, this does not mean that lizardite formed during exhumation, as petrological observations clearly show lizardite formation before prograde metamorphism (Fig. 4a, b, c).

The Shaliuhe serpentinite has light REE that is significantly more enriched than modelled melting residue (Fig. 6a), indicating refertilization either by melt prior to seafloor hydration, or by fluid during serpentinization or subduction. Covariation plots involving Th, REE

**Table 3**
O and Sr isotopic compositions of representative North Qaidam serpentinite and gneiss.

| Sample | | $\delta^{18}O$ (‰) | $^{87}Sr/^{86}Sr$ | SE | Rb (ppm) | Sr (ppm) | $^{87}Rb/^{86}Sr$ | $(^{87}Sr/^{86}Sr)i$ |
|---|---|---|---|---|---|---|---|---|
| Antigorite Serpentinite | 09QL36 | 4.3 | 0.711501 | 0.000010 | 0.113 | 17.9 | 0.018261 | 0.711386 |
| | 09QL37 | 4.1 | 0.711460 | 0.000010 | 0.079 | 6.6 | 0.034639 | 0.711243 |
| | 09QL44 | 4.5 | 0.714044 | 0.000007 | 0.081 | 30.5 | 0.007697 | 0.713996 |
| | 15NQ33 | 4.0 | 0.713205 | 0.000008 | 0.083 | 5.4 | 0.044306 | 0.712927 |
| | 15NQ39 | 4.0 | 0.711317 | 0.000010 | 0.094 | 2.6 | 0.106524 | 0.710649 |
| Lizardite serpentinite | 15NQ43 | 2.7 | 0.708319 | 0.000013 | 0.231 | 6.5 | 0.102605 | 0.707676 |
| | 15NQ44 | 2.4 | 0.708599 | 0.000007 | 0.430 | 5.5 | 0.225809 | 0.707184 |
| | 15NQ45 | 0.6 | 0.709308 | 0.000009 | 0.204 | 4.6 | 0.128664 | 0.708502 |
| Gneiss | 15NQ47 | 10.4 | 0.711895 | 0.000008 | 47.2 | 178.8 | 0.763559 | 0.707109 |
| | 15NQ48 | 9.0 | 0.708120 | 0.000009 | 40.4 | 411.1 | 0.284018 | 0.706340 |

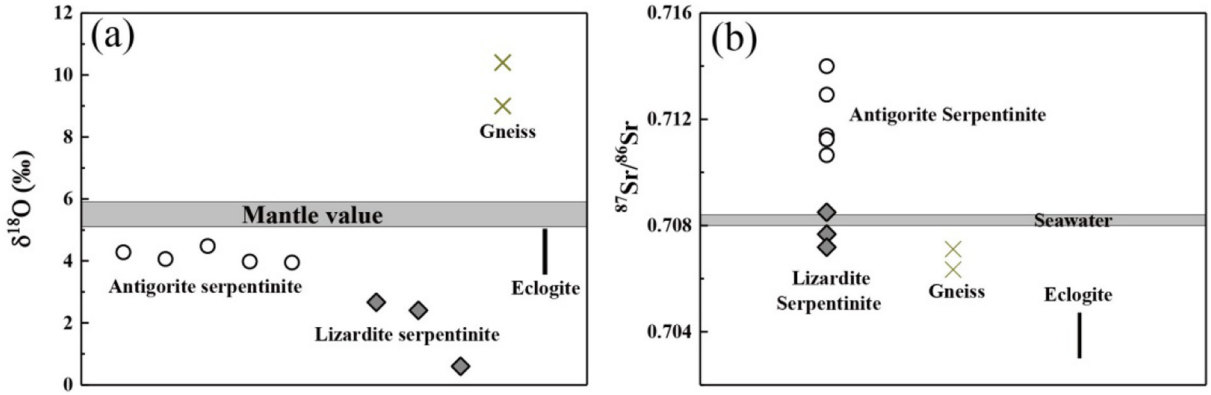


**Fig. 7.** (a) O and (b) Sr isotopic composition of the serpentinite and host rocks. $\delta^{18}O$ of the normal mantle is after Mattey et al. (1994). Sr isotopic data for host eclogite are from Zhang et al., (2017b), and the contemporaneous seawater from Burke et al. (1982).

and HFSE have been used to distinguish between these two processes, based on contrasting behaviors of these elements in fluid and melt (Deschamps et al., 2013; Paulick et al., 2006). In the plot of Th-$(Gd/Yb)_N$ (Fig. 11a), the Shaliuhe serpentinite is shown to have experienced melt injection. The La-Nb plot also demonstrates negligible influence of fluid on REE, as fluid disturbance should cause a deviation from the magmatic trend (Fig. 11b). Therefore, enrichment of light REE and Th in the Shaliuhe serpentinite is due to melt/rock interaction prior to serpentinization. Actually, post-melting refertilization is quite common in abyssal peridotite (Niu, 2004).

Previous studies have suggested that oceanic-type kyanite eclogite and associated serpentinite from Shaliuhe represent coherent subducted oceanic lithosphere (Song et al., 2009; Zhang et al., 2008). Detailed petrological and geochemical investigations on more samples in this study reinforce that protolith of the Shaliuhe serpentinite associated with either oceanic eclogite or continental gneiss is refractory abyssal harzburgite. Considering the tectonic evolution from oceanic subduction to continental subduction in the North Qaidam, the serpentinite is thus most probably derived from oceanic lithosphere that existed before continental subduction (Song et al., 2014; Zhang et al., 2008). In this regard, serpentinite hosted in gneiss represents allochthon emplaced into subducted continental crust, which is also manifested by the sharp contact between the gneiss and enclosed serpentinite. In contrast, the conformable oceanic-type eclogite and associated serpentinite probably represent coherent lower ophiolitic unit, however this needs to be further verified.

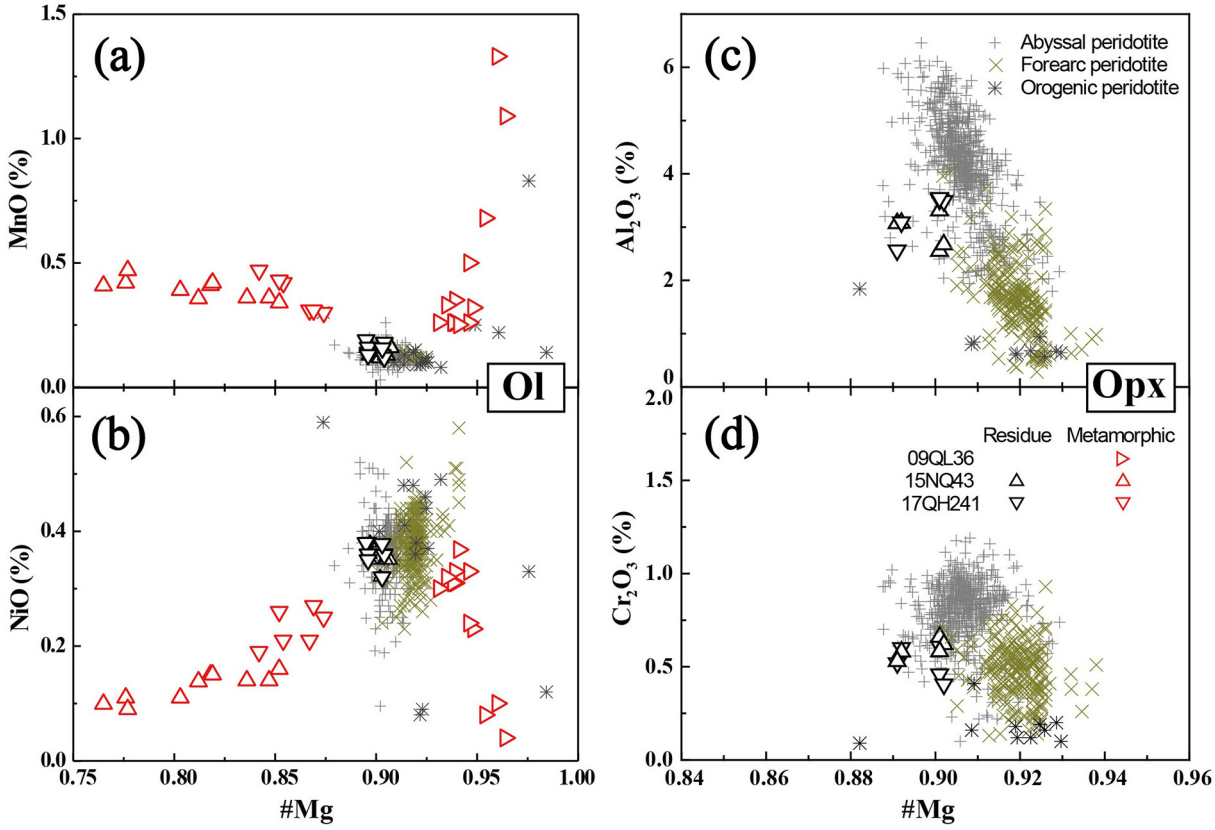


**Fig. 8.** (a) MnO and (b) NiO versus Mg# diagrams for olivine, and (c) $Al_2O_3$ and (d) $Cr_2O_3$ versus Mg# diagrams for orthopyroxene in the serpentinite. The data for abyssal peridotite are from Warren (2016), forearc peridotite are from Ishii et al. (1992), Parkinson and Pearce (1998), and Pearce et al. (2000), and Lüliangshan orogenic peridotite are from Song et al. (2007), Yang and Powell (2008), and Xiong et al. (2015).

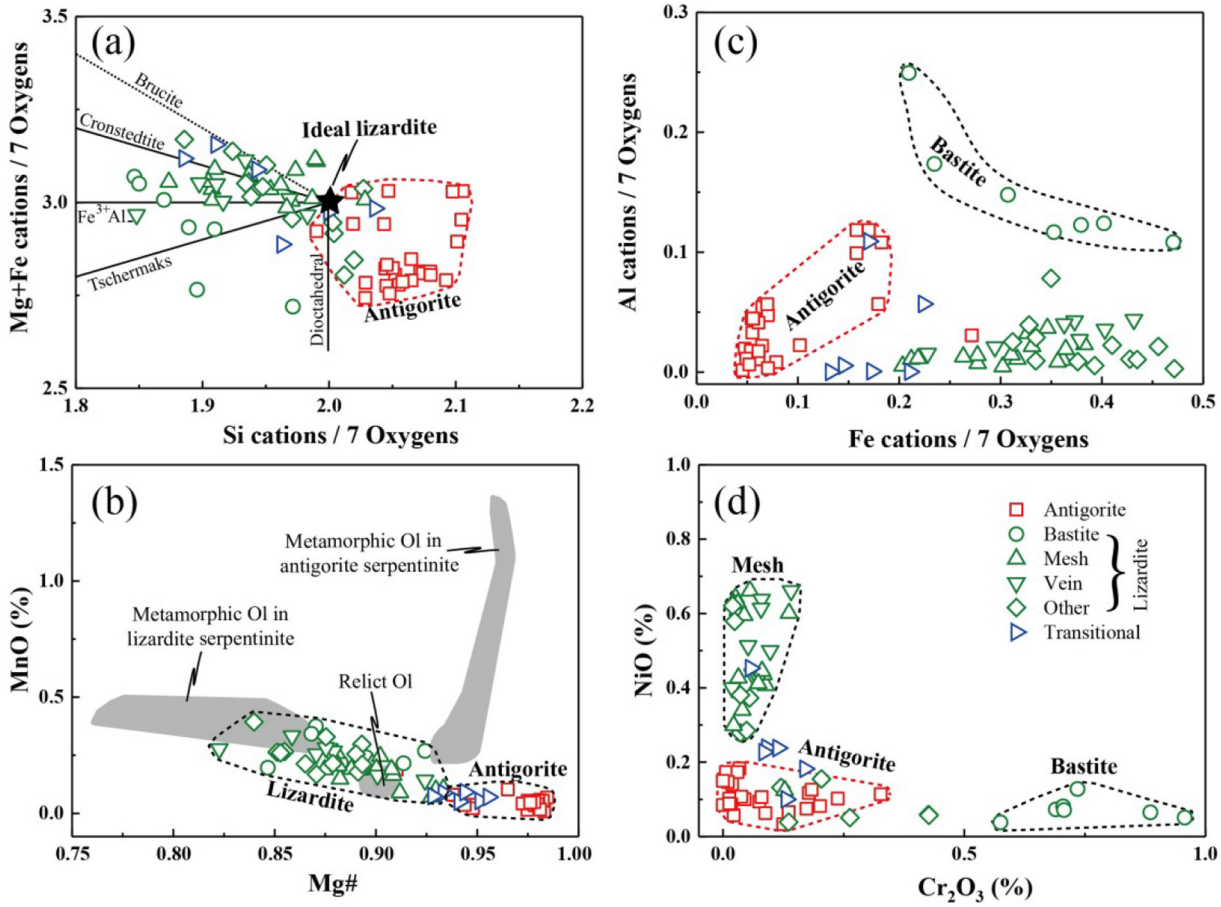


**Fig. 9.** Plots of microprobe data for serpentine. (a) Mg + Fe apfu versus Si apfu. (b) MnO versus Mg#. (c) Al apfu versus Fe apfu. (d) NiO versus $Cr_2O_3$. Vein lizardite represents lizardite in tremolite veinlet; other lizardite represents lizardite without apparent parent minerals; transitional serpentine represents serpentine neighboring secondary olivine in 15NQ43 and 17QH241. The substitution trends in (a) are after Beard and Frost (2016).

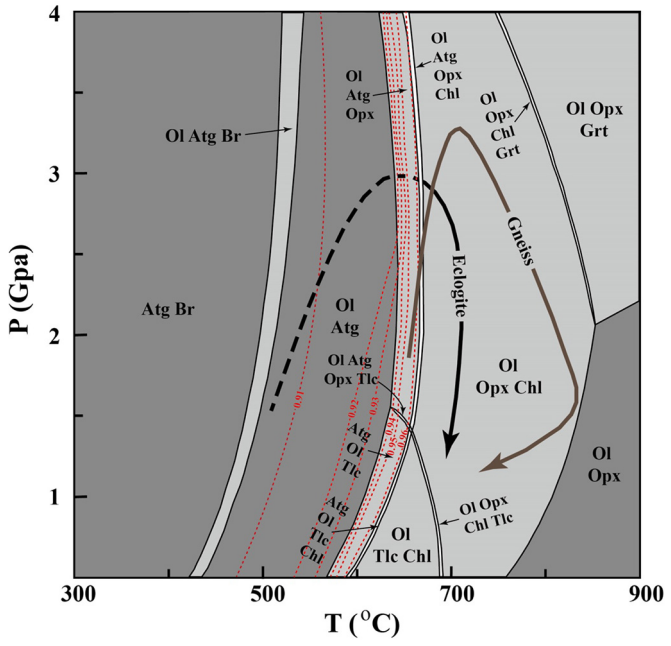


**Fig. 10.** Fluid-saturated P-T pseudosection in the FeO-MgO-$Al_2O_3$-$SiO_2$-$H_2O$ system for antigorite serpentinite 09QL36. The red dashed lines labelled with numbers represent isopleth of olivine Mg#. The black bold line labelled eclogite represents P-T path for nearby eclogite from Zhang et al. (2009), and the grey bold line labelled gneiss represents P-T path for nearby gneiss from Ren et al. (2016).

### 5.2. Petrological evolution of the serpentinite

#### 5.2.1. Serpentinization during seafloor hydration

Textures of initial serpentinization are typified by canonical reactions of olivine to mesh lizardite and magnetite (Fig. 3a, b), and orthopyroxene to bastitic lizardite and talc (Fig. 3c, d). It has been suggested that hydration of olivine occurs stepwise, with formation of iron-rich lizardite and brucite followed by their recrystallization and appearance of magnetite (Bach et al., 2004, 2006; Beard et al., 2009). Nevertheless, no brucite is detected to be intergrown with lizardite by micro-Raman or compositional analyses, indicating destabilization of early-formed brucite into lizardite and magnetite probably in the presence of aqueous silica derived from hydration of pyroxenes (Bach et al., 2006). The close association of tremolite with lizardite indicates that tremolite was also a product of harzburgite hydration. Because of its high Ca content, tremolite in serpentinite is usually considered as a phase produced during hydration of clinopyroxene (Allen and Seyfried Jr., 2003; Frost and Beard, 2007; Klein et al., 2013). The lizardite-tremolite veinlet thus represents conduit of Ca loss during dissolution of clinopyroxene, which acts as source of Ca during the formation of rodingite. Chlorite in the serpentinite always coats ferritchromite (Fig. 3g, h), and it is not in equilibrium with antigorite, but breaks down into antigorite in the antigorite serpentinite (Fig. 3h). This suggests that chlorite and chromite were also produced during harzburgite hydration, probably linked to alteration of Al-spinel as it can act as a source for Cr, Fe, and Al.

It has been shown that temperature plays a key role in dictating the rate of mineral hydrolysis during serpentinization (Allen and Seyfried Jr., 2003; Bach et al., 2004). Pyroxene replacement by talc, tremolite,

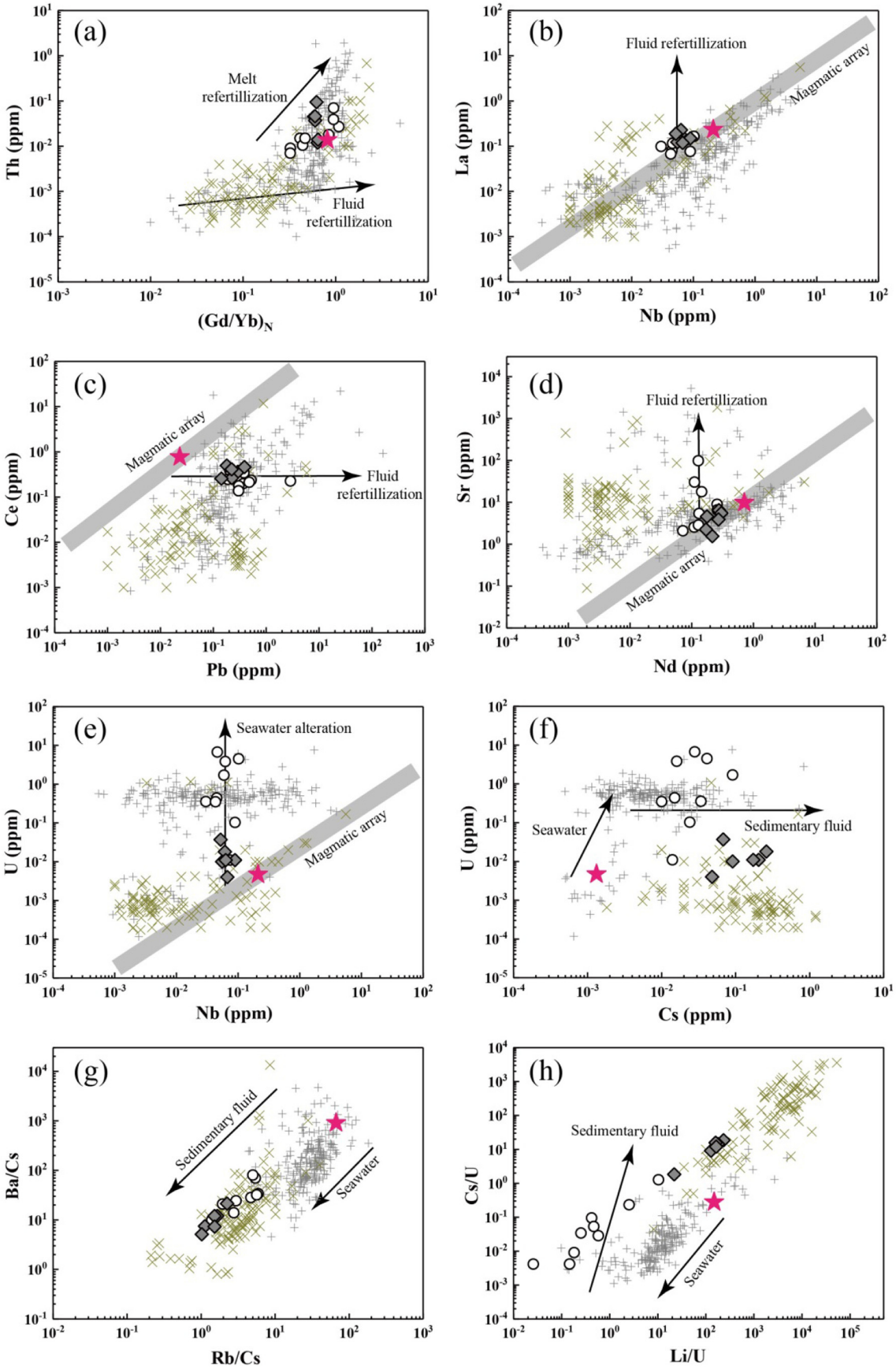


**Fig. 11.** Covariation diagrams of (a) Th versus $(Gd/Yb)_N$, (b) La versus Nb, (c) Ce versus Pb, (d) Sr versus Nd, (e) U versus Nb, (f) U versus Cs, (g) Ba/Cs versus Rb/Cs, (h) Cs/U versus Li/U for the serpentinite. The symbols are same as Fig. 5. Data for abyssal serpentinite and forearc serpentinite are from Peters et al. (2017). The magmatic arrays are fitted after oceanic basalts from PetDB database (http://www.earthchem.org/petdb).

and serpentine is favored at temperatures >350–400 °C when olivine is relatively inert (Allen and Seyfried Jr., 2003; Bach et al., 2004; Klein et al., 2013). Therefore, presence of talc, tremolite, and lizardite after pyroxenes in the Shaliuhe lizardite serpentinite indicates hydration of original harzburgite initiated at temperatures >350–400 °C. This is supported by the fact that formation of chlorite through spinel hydration is also a high-temperature process (>400 °C; Mellini et al., 2005). Low $\delta^{18}O$ of the serpentinite also indicates that original harzburgite had experienced high-temperature hydrothermal alteration. When temperatures dropped to 200–300 °C, hydration of olivine became efficient and magnetite crystallization was favored (Evans, 2010; Klein et al., 2009, 2013, 2014).

*5.2.2. Breakdown of lizardite into antigorite in the serpentinite*

Lizardite is gradually replaced by antigorite in the Shaliuhe serpentinite (Fig. 4). Antigorite replacing lizardite is commonplace in both recrystallized abyssal serpentinite (Rouméjon et al., 2015, 2018) and subducted serpentinite (Schwartz et al., 2013). However, antigorite in both the lizardite serpentinite and antigorite serpentinite from Shaliuhe has textures different from antigorite in recrystallized abyssal serpentinite (Rouméjon et al., 2015, 2018). Considering the close association of Shaliuhe serpentinite with UHP metamorphic rocks, it is preferred that breakdown of lizardite into antigorite in the Shaliuhe serpentinite occurred during subduction zone metamorphism. The two most common proposed reactions for growth of antigorite at the expense of lizardite are (Evans, 2004):

$$\text{lizardite} \rightarrow \text{antigorite} + \text{brucite} \quad (1)$$

or

$$\text{lizardite} + SiO_{2,aq} \rightarrow \text{antigorite} + \text{fluid} \quad (2)$$

They correspond to lizardite/antigorite transformation in a closed system or in an open system with external aqueous silica, respectively (Evans, 2004; Kodolányi and Pettke, 2011; Schwartz et al., 2013). In the Shaliuhe lizardite serpentinite, mesh or bastitic lizardite is commonly replaced by interconnected antigorite networks or veinlets along boundaries (Fig. 4a, b). Moreover, no brucite has been detected to coexist with antigorite. These observations suggest that breakdown of lizardite into antigorite is probably fluid-assisted through reaction (2). Nevertheless, reaction (1) may be responsible for growth of antigorite in serpentinite such as 09QL36, as brucite is necessary for generation of magnesian secondary olivine during partial breakdown of antigorite (Section 5.2.3). It can be deduced from reaction (2) that antigorite is more enriched in silica than lizardite, which is in accordance with actual analyses (Fig. 9a). Besides, antigorite has lower FeO than lizardite, which contradicts with the idea that Fe released during magnetite dissolution should be transferred to antigorite (Debret et al., 2014). This indicates that magnetite is not necessarily destroyed during breakdown of lizardite into antigorite, in accordance with the observation that magnetite can remain its original outline even in the antigorite serpentinite. Some chromite grains are closely associated with antigorite formation (Fig. 4b), instead of being product of spinel alteration that is coated by chlorite. Therefore, these chromite grains may serve as the sink for excess Fe during growth of antigorite from lizardite.

*5.2.3. Appearance of secondary olivine in the serpentinite*

Antigorite transformed from lizardite would progressively decompose during subsequent subduction of serpentinite. In general, a minor fraction of antigorite would first break down through the following reaction to form secondary olivine (Evans, 2004):

$$\text{antigorite} + \text{brucite} \rightarrow \text{olivine} + \text{fluid} \quad (3)$$

Remaining antigorite would later completely dehydrate into olivine and enstatite (Evans, 2004; Ulmer and Trommsdorff, 1995). Metamorphic olivine is observed in antigorite serpentinite 09QL36 and lizardite serpentinite 15NQ43 and 17QH241, whereas no metamorphic orthopyroxene is identified. Therefore, only the olivine-in reaction curve was intersected by P-T path of the serpentinite. Besides texture, metamorphic olivine can also be distinguished from relict olivine by its higher MnO, lower NiO, and different Mg# (Fig. 8a, b). High MnO is widely reported for metamorphic olivine in subducted serpentinite from other orogens (Debret et al., 2013b; Li et al., 2004; López Sánchez-Vizcaíno et al., 2005; Padrón-Navarta et al., 2011; Rebay et al., 2012; Scambelluri et al., 1991; Shen et al., 2015; Trommsdorff et al., 1998). This is due to preferential partition of Mn into olivine relative to coexisting antigorite, as shown by lower MnO in antigorite when compared with olivine and lizardite (Fig. 9b). Metamorphic olivine in the Shaliuhe serpentinite shows a wide range of Mg#. Secondary olivine in 09QL36 has Mg# higher than relict olivine, while secondary olivine in 15NQ43 and 17QH241 has Mg# lower than relict olivine. Previous studies have also reported secondary olivine with a large variation of Mg# in subducted serpentinite (Bretscher et al., 2018; Debret et al., 2013b; Li et al., 2004; Rebay et al., 2012; Scambelluri et al., 1991; Shen et al., 2015), which is generally ascribed to highly variable reactive bulk rock Mg# dependent on the amount of non-reactive relict magnetite (Bretscher et al., 2018).

In antigorite serpentinite, iron is mainly distributed among antigorite and magnetite. Antigorite has higher Mg# than relict olivine as a significant amount of iron is incorporated in magnetite (Fig. 9b). Partial decomposition of antigorite through reaction (3) without the participation of magnetite would produce secondary olivine with Mg# higher than relict olivine. Instead, secondary olivine can be Fe-rich if magnetite is involved in its formation (Bretscher et al., 2018; Merkulova et al., 2016, 2017). Consumption of magnetite to form very ferroan olivine has been well illustrated by contact-metamorphosed serpentinite (Arai, 1975; Nozaka, 2003, 2005). Therefore, high Mg# secondary olivine in antigorite serpentinite 09QL36 indicates that magnetite was not involved in breakdown of antigorite. This is reinforced by the observation that magnetite arrays remain polygonal outline in 09QL36 and are thus probably not reactive. It is proposed that extended stability of magnetite in subducted serpentinite is boosted by Cr incorporation into magnetite (Debret et al., 2014; Merkulova et al., 2016, 2017). However, inertness of magnetite in the Shaliuhe serpentinite is probably due to kinetic barriers, as the magnetite contains little Cr.

In contrast with secondary olivine in 09QL36, secondary olivine in lizardite serpentinite 15NQ43 and 17QH241 has Mg# lower than relict olivine. This intuitively indicates participation of magnetite during formation of secondary olivine, as discussed above. Nevertheless, only minor network and veinlet antigorite, without the coexistence of brucite, is present in 15NQ43 and 17QH241. Moreover, serpentine neighboring secondary olivine in 15NQ43 and 17QH241 is mostly transitional serpentine. Therefore, breakdown of antigorite through reaction (3) along with magnetite into ferroan secondary olivine is unlikely. Secondary olivine in 15NQ43 occupies the site of original mesh lizardite (Fig. 4e, f), and secondary olivine in 17QH241 occurs in original bastite pseudomorph (Fig. 4g, h). Patches of secondary olivine and neighboring serpentine are further surrounded by lizardite and tremolite (Fig. 4e, g). Composition integrating secondary olivine and neighboring serpentine in 15NQ43 and 17QH241 closely resemble that of mesh and bastitic lizardite, respectively. All these observations imply that secondary olivine in these samples was probably generated by direct breakdown of metastable lizardite through the reaction (Dungan,

1977; Evans, 2004):

$$\text{lizardite (mediate—Fe)} = \text{antigorite (low—Fe)} + \text{olivine (high—Fe)} + \text{fluid} \quad (4)$$

This reaction efficiently explains the texture of secondary olivine and the intermediate Mg# of lizardite compared with those of antigorite and secondary olivine (Fig. 9b). Nevertheless, the transformation of lizardite into antigorite through reaction (4) may not be complete, with serpentine neighboring secondary olivine transitional between lizardite and antigorite.

It is questionable whether the texture of ferroan olivine and neighboring serpentine can be produced by hydration of ferroan secondary olivine. However, the ferroan secondary olivine is highly anhedral with greatly varying size, in contrast to relict olivine in mesh core that is generally oval (Fig. 4e, f, g and h). Moreover, serpentine neighboring the secondary olivine is not lizardite and its rim is not surrounded by magnetite (Fig. 4e, f, g and h). Besides, secondary olivine in 17QH241 is oriented and talc is detected in the orthopyroxene pseudomorph (Fig. 4g, h), both observations being uncommon during olivine hydration. Therefore, it is concluded that the texture was produced by breakdown of lizardite into olivine, not vice versa.

*5.2.4. Metastability of lizardite in subducted serpentinite*

It is highly unusual that high amounts of oceanic lizardite in the Shaliuhe serpentinite survived high-grade metamorphism, as lizardite is not stable and should transform into antigorite during subduction. Therefore, it is possible that the lizardite formed as a retrograde product with fluid input from country rock and exchange with meteoric water, which can also explain the low $\delta^{18}O$ and elevated FME of the lizardite serpentinite (Scicchitano et al., 2018). Nevertheless, this possibility can be excluded by the petrological observations of lizardite mainly replacing mantle olivine and orthopyroxene (Fig. 3a, c) and antigorite further replacing the lizardite along periphery (Fig. 4a, b, c). Moreover, the texture of ferroan secondary olivine and neighboring serpentine in the lizardite serpentinite is quite different from serpentinization mesh texture, as described in the above discussion. $^{87}Sr/^{86}Sr$ of serpentinite, higher than its country rocks (Fig. 7b), also implies limited fluid input from country rocks during exhumation. Besides, it is also unlikely that meteoric water can penetrate into great depths in subduction zones. Therefore, lizardite in the Shaliuhe serpentinite mainly formed during seafloor serpentinization and remained metastable during subduction.

In fact, survival of minerals and textures formed during seafloor serpentinization is common in subducted serpentinite, e.g., serpentinized peridotite in undeformed domains from Erro-Tobbio Unit, Ligurian Alps (Früh-Green et al., 2001; Scambelluri et al., 1991). In the Erro-Tobbio, serpentinite in the undeformed domain retains seafloor serpentinization textures, with lizardite as the dominant serpentine species. The undeformed serpentinite contains little high-pressure minerals, with only minor antigorite replacing lizardite in network and veinlet. In contrast, serpentinite in the deformed domain has recrystallized with HP eclogite-facies paragenesis of dominantly olivine and antigorite. Overall, the Erro-Tobbio serpentinite is similar to the Shaliuhe serpentinite, considering that the Shaliuhe lizardite serpentinite is undeformed and massive, while the Shaliuhe antigorite serpentinite is deformed and foliated. In this regard, deformation and associated fluid activity may have been crucial in dictating the metastability of lizardite and other minerals formed during seafloor serpentinization. This is plausible as recrystallization during metamorphism is usually promoted by deformation and fluid. $^{87}Sr/^{86}Sr$ of the antigorite serpentinite, which is higher than the lizardite serpentinite, also indicates that the former has more access to fluid than the latter. Hence, preservation of high amounts of lizardite in the Shaliuhe serpentinite is due to limited deformation and fluid availability during subduction. For overheating lizardite, an alternative terminal is reaction (4), which produces ferroan secondary olivine and releases fluid (Dungan, 1977; Evans, 2004). Nevertheless, only rare lizardite have overcome reaction energy barrier and dehydrated into olivine, while most lizardite remains metastable.

*5.2.5. P-T condition of the serpentinite*

It is difficult to reconstruct the P-T path of the Shaliuhe serpentinite as the serpentinite was not fully equilibrated in response to subduction, and mineral assemblage of serpentinite is usually simple and stable under a wide variety of P-T conditions. In antigorite serpentinite 09QL36, the assemblage of olivine-antigorite is stable at approximately 500–600 °C, which is much lower than peak temperatures constructed from nearby eclogite and gneiss (Fig. 10). At the temperatures recorded by nearby eclogite and gneiss, the serpentinite is expected to dehydrate into harzburgite (Fig. 10). Three possible scenarios may be responsible for the discrepancy: (1) the serpentinite has a separate evolution from the eclogite and the gneiss, and they were juxtaposed together during exhumation. (2) The original serpentinite had dehydrated into secondary peridotite and then rehydrated into serpentinite during exhumation. (3) Temperatures constructed previously from eclogite and gneiss were overestimated and are actually consistent with olivine-antigorite stability in the serpentinite. The second possibility is not favored, as metamorphic olivine and antigorite are in equilibrium in 09QL36. In addition, no secondary orthopyroxene is found in the serpentinite. The serpentinite hosted in gneiss was probably emplaced during exhumation, as it is in sharp contact with host gneiss (Fig. 2c). However, the eclogite and enclosed serpentinite constitute a conformable unit (Fig. 2b), indicating coherent evolution. Therefore, the third scenario is possible, however further thermobarometric studies on nearby eclogite and gneiss are needed to verify this.

*5.3. Geochemical behaviors of elements in the serpentinite*

*5.3.1. Stepwise enrichment of FME in the serpentinite*

The Shaliuhe serpentinite mostly inherits the major element composition of its protolith harzburgite. Nevertheless, some samples experienced significant Ca loss during hydration, as evidenced by their low Ca contents (Fig. 5d). Besides, the Shaliuhe serpentinite was also subjected to Mg loss during seafloor weathering, as the samples plot below the terrestrial array on the diagram of $MgO/SiO_2$ versus $Al_2O_3/SiO_2$ (Fig. 5e; Snow and Dick, 1995; Niu, 2004). The most significant characteristic of the Shaliuhe serpentinite is its enrichment in FME, notably Pb, U, and Cs (Fig. 6b; Fig. 11c, e, f). FME notably deviate from magmatic trends in Fig. 11, indicating their enrichment during either serpentinization on seafloor or metamorphism in subduction channel at prograde or retrograde stages (Pelletier et al., 2008; Deschamps et al., 2010, 2011, 2012; Kodolányi et al., 2012; Debret et al., 2013a; Lafay et al., 2013; Barnes et al., 2014; Cannaò et al., 2016). As the serpentinite is abyssal in origin, it is without doubt that the serpentinite was selectively enriched in FME (notably U and Pb) during alteration on seafloor (Fig. 6b; Fig. 11c, e, f). However, it is essential to evaluate whether element budgets of the serpentinite were overprinted by fluid influx from external sources, such as sediments (Cannaò et al., 2016; Debret et al., 2013a; Deschamps et al., 2010, 2011, 2012; Lafay et al., 2013).

Recent geochemical compilations on abyssal and forearc serpentinite have demonstrated that serpentinization in abyssal setting give rise to apparent U enrichment due to high U mobility under oxidized condition on seafloor, and serpentinization in the mantle wedge by sedimentary fluids leads to conspicuous Cs enrichment due to high Cs input in sedimentary fluids (Deschamps et al., 2013; Peters et al., 2017). In this regard, Cs-U systematics can be applied to recognizing imprint of sedimentary fluids in subducted abyssal serpentinite. The Shaliuhe serpentinite samples have elevated U contents, which is typical of seafloor alteration (Fig. 11e). However, they straddle between abyssal serpentinite and forearc serpentinite in the plot of U versus Cs (Fig. 11f), indicating fluid input from sediments. The signature of

sediments is even more obvious in the plot of Ba/Cs-Rb/Cs, with the Shaliuhe serpentinite completely overlapping with forearc serpentinite (Fig. 11g). Sr isotopes of the Shaliuhe serpentinite, which is more radiogenic than those of contemporaneous seawater and host rocks, also implies interaction with fluids derived from sediments with highly radiogenic Sr (Fig. 7b). Therefore, FME enrichment in the Shaliuhe serpentinite is a two-step process, with elevation of U during abyssal serpentinization followed by further concentration of Cs during interaction with sedimentary fluids (Fig. 11f, g, h). Li, Rb and Ba behave linearly with Cs (Fig. 11g, h), but their enrichment is far more limited (Fig. 6b).

Interaction of abyssal serpentinite with fluids once equilibrated with sediments can occur at bending faults on seafloor, in accretionary wedge during subduction and in subduction channel during exhumation (Cannaò et al., 2016; Deschamps et al., 2012; Lafay et al., 2013). Interaction with host rocks during exhumation can be excluded as the serpentinite has higher $^{87}Sr/^{86}Sr$ than nearby eclogite and granitic gneiss. Outer rise close to trench zone is one possible site for contamination of abyssal serpentinite by sediments, where large amounts of sediments can accumulate and fluids equilibrated with sediments can easily infiltrate the serpentinite along bending faults (Cannaò et al., 2016; Deschamps et al., 2011, 2012). Moreover, normal faults formed due to bending of oceanic slab before sinking into subduction zone are also ideal sites for second-stage serpentinization of oceanic mantle peridotite, and the infiltrating fluids are mixtures of seawater and sedimentary fluids (Cannaò et al., 2016; Deschamps et al., 2011, 2012). Plenty of sediments can also accumulate in the accretionary wedge and extend downward deeply along the plate-slab interface, which can expulse fluids to react with subducted serpentinite (Cannaò et al., 2016; Deschamps et al., 2011, 2012 ; Lafay et al., 2013). The presence of sedimentary fingerprint in the Shaliuhe lizardite serpentinite (Fig. 11f, g, h) indicates influx of sediments-derived fluids in the outer rise environment or in the accretionary wedge before lizardite transformation into antigorite. Petrological observations demonstrate that breakdown of lizardite into antigorite is mostly fluid-assisted, which is probably linked to infiltration of sedimentary fluids in the accretionary wedge. Overall, FME uptake from sediments in the Shaliuhe serpentinite in either the bending faults or the accretionary wedge is possible and it is difficult to quantify their relative role.

*5.3.2. Release of FME during dehydration of the serpentinite*

Significant contrast exists between the FME systematics of the lizardite serpentinite and antigorite serpentinite. The lizardite serpentinite mostly has lower U and higher Li, Cs, Rb, and Ba than the antigorite serpentinite (Fig. 11e, f, g, h). The contrast is not due to protolith heterogeneity, as the two types of serpentinite have similar geochemical compositions except for FME. Therefore, differences in serpentinization condition and subduction zone reworking are responsible for the discrepancy. Their contrast in U should be caused by different serpentinization degrees on the seafloor, as the antigorite serpentinite was completely hydrated, while the lizardite serpentinite was less hydrated with abundant relict mantle minerals. As discussed above, FME and Sr isotopes of both the lizardite serpentinite and antigorite serpentinite indicate that they have interacted with sedimentary fluids. Compared with the lizardite serpentinite, the antigorite serpentinite should have interacted more intensely with sedimentary fluids, as it is more deformed. This is also demonstrated by higher $^{87}Sr/^{86}Sr$ of the antigorite serpentinite when compared with the lizardite serpentinite. Different extents of interaction with fluids from sediments may be ascribed to disparate positions of the lizardite serpentinite and antigorite serpentinite, with the former situated deeper in the oceanic lithosphere as the amount of sedimentary fluids decreases rapidly with depth. This can also explain incomplete serpentinization and lower U of the lizardite serpentinite, as infiltration of seawater into oceanic lithosphere during peridotite hydration is subdued at depth.

As the deformed antigorite serpentinite interacted more intensely with sedimentary fluids, it was expected to contain higher Li, Cs, Rb, and Ba than the undeformed lizardite serpentinite before subduction (Cannaò et al., 2016). However, the antigorite serpentinite has lower Li, Cs, Rb, and Ba than the lizardite serpentinite, which indicates release of these elements during dehydration of the antigorite serpentinite. Probable episodes of dehydration with release of FME are transformation of lizardite into antigorite and appearance of secondary olivine (Debret et al., 2013a; Kodolányi and Pettke, 2011; Lafay et al., 2013; Scambelluri et al., 2001, 2004a, 2004b). It is difficult to distinguish element release between these two dehydration episodes in the Shaliuhe serpentinite. However, previous studies have shown that serpentinite can act as a sponge for FME before initiation of antigorite decomposition (Deschamps et al., 2011, 2012; Lafay et al., 2013), although some elements such as B and Cl can be released during breakdown of lizardite into antigorite (Debret et al., 2013a; Kodolányi and Pettke, 2011; Lafay et al., 2013). Therefore, Li, Cs, Rb, and Ba were probably released during appearance of secondary olivine by partial breakdown of antigorite. In contrast, the antigorite serpentinite has similar U to common abyssal serpentinite, which is higher than the lizardite serpentinite (Fig. 11e, f). This indicates conservation of U during partial

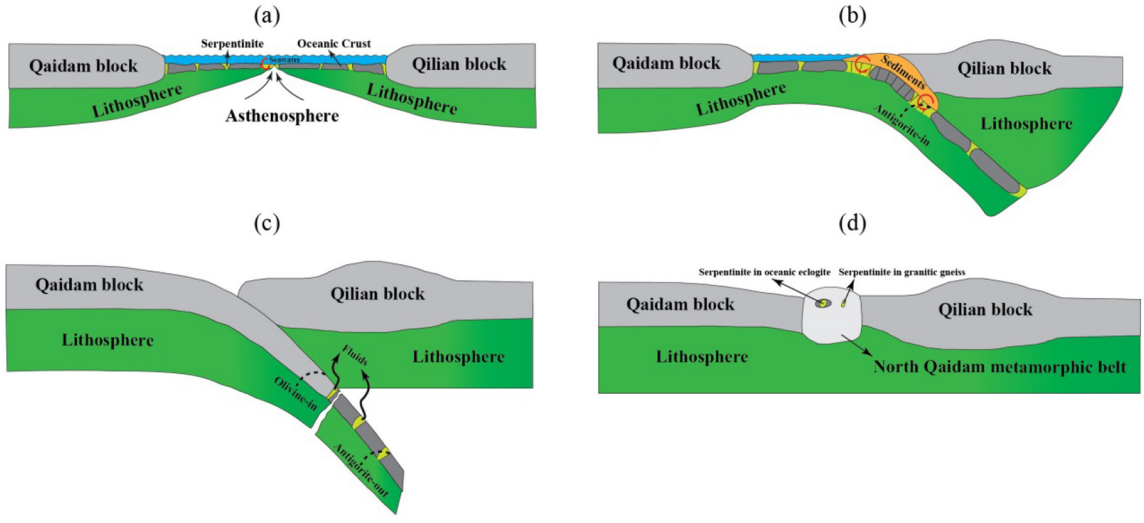


**Fig. 12.** A schematic sketch showing evolution of the serpentinite from seafloor alteration to subduction zone metamorphism in the context of the North Qaidam tectonics. Detailed descriptions of each stage are provided in Section 6.

antigorite decomposition. It can be inferred that element mobility in fluid released by partial antigorite dehydration in subducted serpentinite follows the order of Cs > Li > Rb, Ba > U, by comparing the relative depletion of FME in the antigorite serpentinite with the lizardite serpentinite. Assuming that the antigorite serpentinite and lizardite serpentinite had similar FME before subduction, a simple ratio between them indicates that about 80% Cs and Li and 50%–60% Rb and Ba were released during dehydration on average. However, this estimate should be an upper limit, as the antigorite serpentinite was originally expected to have higher FME than the lizardite serpentinite due to more intense interaction with sedimentary fluids.

*5.3.3. Implications for FME systematics of subducted serpentinite*

Strikingly, this and previous studies show that nearly all subducted serpentinite displays imprints of sedimentary fluids (Cannaò et al., 2016; Deschamps et al., 2010, 2012, 2013; Hattori and Guillot, 2007; Lafay et al., 2013; Peters et al., 2017), which has been viewed as evidence for slab-mantle interaction at plate interface (Cannaò et al., 2016). Nevertheless, enrichment of FME in the Shaliuhe lizardite serpentinite that is not severely disturbed by subduction zone metamorphism indicates that subducted serpentinite can acquire sedimentary components at shallow depth. Moreover, the characteristics can be retained during subduction, although enrichment of some FME is subdued due to release upon dehydration. In this regard, enrichment of FME in subducted serpentinite is not exclusive to slab-mantle interaction in deep subduction channel. Concentrations of most FME in subducted serpentinite are low when compared with other lithology in subduction zones. Moreover, large proportions of FME are released during transformation of lizardite into antigorite and partial decomposition of antigorite into olivine. Therefore, complete dehydration of serpentinite at subarc depth is probably not a crucial source for FME, except for a few elements (Spandler et al., 2014; Tenthorey and Hermann, 2004). Nevertheless, subducted serpentinite can still serve as a significant reservoir of water and other volatiles for arc magmatism (Alt et al., 2013; Spandler and Pirard, 2013).

## 6. Evolution of serpentinite from seafloor hydration to subduction zone metamorphism

Comprehensive knowledge on the evolution of the Shaliuhe serpentinite can be obtained from the petrological observations and geochemical constraints discussed above. The key stages are summarized below and illustrated in Fig. 12:

(a) Depleted oceanic harzburgite was produced during opening of oceanic basin between the Qaidam block and the Qilian block. Harzburgite exposed on seafloor experienced various degrees of serpentinization upon infiltration by seawater, with reactions of olivine to lizardite and magnetite (Fig. 3a, b), pyroxenes to lizardite, talc, and tremolite (Fig. 3c, d, e, f), and Al-spinel to chromite and chlorite (Fig. 3g). The serpentinite lost Ca during hydration (Fig. 5d), whereas it was enriched in water and some FME (notably U, Pb, and Cs; Fig. 11c, e, f). Harzburgite situated deeper in the lithosphere was less accessible to seawater and underwent lower degrees of hydration, with survival of numerous relict mantle minerals and subdued enrichment in FME. The serpentinite lost some Mg during residence on seafloor, leading to lower $MgO/SiO_2$ when compared with the terrestrial array (Fig. 5e).

(b) A subduction zone developed at the northern margin of the oceanic basin, and the oceanic slab started to subduct beneath the Qilian block. The serpentinite interacted with fluids equilibrated with sediments at the outer rise or in the accretionary wedge when sinking into the subduction zone, with further elevation of some FME (notably Cs, Li, Rb, and Ba; Fig. 11f, g, h). With continued subduction, lizardite broke down into antigorite in deformed domains. In contrast, lizardite in undeformed serpentinite mostly remained metastable.

(c) Continental crust of the Qaidam block was also dragged down into subduction zone by the pull of sinking oceanic slab. The antigorite serpentinite reached olivine-in thermal condition and Mg-rich secondary olivine was produced by partial decomposition of antigorite. Cs, Li, Rb, and Ba were released during the partial dehydration of antigorite, while U was relatively immobile. In contrast, only sporadic Fe-rich secondary olivine occurred in the lizardite serpentinite due to direct breakdown of metastable lizardite.

(d) The majority of subducted oceanic slab broke off from the subducted continental slab, and the latter exhumed towards the surface. Minor oceanic eclogite and serpentinite attached to the continental crust were also uplifted and emplaced into the continental crust. Exhumed serpentinite may still be associated with oceanic eclogite, or decoupled from oceanic eclogite and emplaced into granitic gneiss.

## 7. Conclusions

Petrological and geochemical studies revealed information about the protolith nature, serpentinization process, and subduction zone metamorphism of Shaliuhe serpentinite from the North Qaidam orogen. The serpentinite has bulk rock and relict mineral compositions similar to abyssal serpentinite, which was probably produced in the oceanic basin that subducted before continental subduction. Minerals and textures related to serpentinization can persist to great depths in subduction zones in undeformed domains. The transition of lizardite into antigorite with the assistance of external fluid may be common in subduction zones. Fe-rich secondary olivine can form directly by decomposition of metastable lizardite, in stark contrast to Mg-rich secondary olivine produced by partial breakdown of antigorite. Subducted serpentinite is enriched in FME during hydration on seafloor and infiltration by fluids equilibrated with sediments at bending faults or in accretionary wedge. The enrichment of FME can be retained in subducted serpentinite, but some FME such as Cs, Li, Rb and Ba are released during dehydration of serpentinite.

Supplementary data to this article can be found online at https://doi.org/10.1016/j.lithos.2019.105158.

## Acknowledgements

This study was supported by funds from the National Key R & D Program of China (2016YFC0600408), the Strategic Priority Research Program of the Chinese Academy of Sciences (XDB18000000), the Natural Science Foundation of China (41703029), and the China Postdoctoral Science Foundation (2016LH00023). We are grateful to Hermann, J. and an anonymous reviewer for their thorough reviews that greatly improved the presentation of the manuscript. The editorial handling of Scambelluri, M. is also highly appreciated. This is contribution No. IS-2734 from GIGCAS.

## References

Allen, D.E., Seyfried Jr., E., 2003. Compositional controls on vent fluids from ultramafic-hosted hydrothermal systems at mid-ocean ridges: an experimental study at 400°C, 500 bars. Geochim. Cosmochim. Acta 67, 1531–1542.

Alt, J.C., Shanks, W.C., 2006. Stable isotope compositions of serpentinite seamounts in the Mariana forearc: serpentinization processes, fluid sources and sulfur metasomatism. Earth Planet. Sci. Lett. 242, 272–285.

Alt, J.C., Schwarzenbach, E.M., Früh-Green, G.L., Shanks, W.C., Bernasconi, S.M., Garrido, C.J., Crispini, L., Gaggero, L., Padrón-Navarta, J.A., Marchesi, C., 2013. The role of serpentinites in cycling of carbon and sulfur: seafloor serpentinization and subduction metamorphism. Lithos 178, 40–54.

Arai, S., 1975. Contact metamorphosed dunite-harzburgite complex in the Chigoku district, western Japan. Contrib. Mineral. Petrol. 52, 1–16.

Bach, W., Garrido, C.J., Paulick, H., Harvey, J., Rosner, M., 2004. Seawater–peridotite interactions: first insights from ODP Leg 209, MAR 15°N. Geochem. Geophys. Geosyst. 5. https://doi.org/10.1029/2004GC000744.

Bach, W., Paulick, H., Garrido, C.J., Ildefonse, B., Meurer, W.P., Humphris, S.E., 2006. Unraveling the sequence of serpentinization reactions: petrography, mineral chemistry and petrophysics of serpentinites from MAR 15°N (ODP Leg 209, Site 1274). Geophys. Res. Lett. 33. https://doi.org/10.1029/2006GL025681.

Barnes, J.D., Beltrando, M., Lee, C.-T.A., Cisneros, M., Loewy, S., Chin, E., 2014. Geochemistry of Alpine serpentinites from rifting to subduction: a view across paleogeographic domains and metamorphic grade. Chem. Geol. 389, 29–47.

Beard, J.S., Frost, B.R., 2016. The stoichiometric effects of ferric iron substitutions in serpentine from microprobe data. Int. Geol. Rev. 58, 1–7.

Beard, J.S., Frost, B.R., Fryer, P., McCaig, A., Searle, R., Ildefonse, B., Zinin, P., Sharma, S.K., 2009. Onset and progression of serpentinization and magnetite formation in olivine-rich troctolite from IODP Hole U1309D. J. Petrol. 50, 387–403.

Bretscher, A., Hermann, J., Pettke, T., 2018. The influence of oceanic oxidation on serpentinite dehydration during subduction. Earth Planet. Sci. Lett. 499, 173–184.

Burke, W.H., Denison, R.E., Hetherington, E.A., Koepnick, R.B., Nelson, H.F., Otto, J.B., 1982. Variation of seawater $^{87}Sr/^{86}Sr$ throughout Phanerozoic time. Geology 10, 516–519.

Cannaò, E., Agostini, S., Scambelluri, M., Tonarini, S., Godard, M., 2015. B, Sr and Pb isotope geochemistry of high-pressure Alpine metaperidotites monitors fluid-mediated element recycling during serpentinite dehydration in subduction mélange (Cima di Gagnone, Swiss Central Alps). Geochim. Cosmochim. Acta 163, 80–100.

Cannaò, E., Scambelluri, M., Agostini, S., Tonarini, S., Godard, M., 2016. Linking serpentinite geochemistry with tectonic evolution at the subduction plate-interface: the Voltri Massif case study (Ligurian Western Alps, Italy). Geochim. Cosmochim. Acta 190, 115–133.

Chen, R.-X., Li, H.-Y., Zheng, Y.-F., Zhang, L., Gong, B., Hu, Z., Yang, Y., 2017. Crust-mantle interaction in a continental subduction channel: evidence from orogenic peridotites in North Qaidam, Northern Tibet. J. Petrol. 58, 191–226.

Connolly, J., 2005. Computation of phase equilibria by linear programming: A tool for geodynamic modeling and its application to subduction zone decarbonation. Earth Planet. Sci. Lett. 236, 524–541.

Debret, B., Andreani, M., Godard, M., Nicollet, C., Schwartz, S., 2013a. Trace element behavior during serpentinization/deserpentinization of an eclogitized oceanic lithosphere: a LA-ICPMS study of the Lanzo ultramafic massif (Western Alps). Chem. Geol. 357, 117–133.

Debret, B., Nicollet, C., Andreani, M., Schwartz, S., Godard, M., 2013b. Three steps of serpentinization in an eclogitized oceanic serpentinization front (Lanzo Massif – Western Alps). J. Metamorph. Geol. 31, 165–186.

Debret, B., Andreani, M., Muñoz, M., Bolfan-Casanova, N., Carlut, J., Nicollet, C., Schwartz, S., Trcera, N., 2014. Evolution of Fe redox state in serpentine during subduction. Earth Planet. Sci. Lett. 400, 206–218.

Deschamps, F., Guillot, S., Godard, M., Chauvel, C., Andreani, M., Hattori, K., 2010. In situ characterization of serpentinites from forearc mantle wedges: timing of serpentinization and behavior of fluid-mobile elements in subduction zones. Chem. Geol. 269, 262–277.

Deschamps, F., Guillot, S., Godard, M., Andreani, M., Hattori, K., 2011. Serpentinites act as sponges for fluid-mobile elements in abyssal and subduction zone environments. Terra Nova 23, 171–178.

Deschamps, F., Godard, M., Guillot, S., Chauvel, C., Andreani, M., Hattori, K., Wunder, B., France, L., 2012. Behavior of fluid-mobile elements in serpentines from abyssal to subduction environments: examples from Cuba and Dominican Republic. Chem. Geol. 312–313, 93–117.

Deschamps, F., Godard, M., Guillot, S., Hattori, K., 2013. Geochemistry of subduction zone serpentinites: A review. Lithos 178, 96–127.

Dungan, M.A., 1977. Metastability in serpentine-olivine equilibria. Am. Mineral. 62, 1018–1029.

Evans, B.W., 2004. The serpentinite multisystem revisited: Chrysotile is metastable. Int. Geol. Rev. 46, 479–506.

Evans, B.W., 2010. Lizardite versus antigorite serpentinite: Magnetite, hydrogen, and life (?). Geology 38, 879–882.

Evans, B.W., Hattori, K., Baronnet, A., 2013. Serpentinite: what, why, where? Elements 9, 99–106.

Frost, B.R., Beard, J.S., 2007. On silica activity and serpentinization. J. Petrol. 48, 1351–1368.

Früh-Green, G.L., Scambelluri, M., Vallis, F., 2001. O-H isotope ratios of high-pressure ultramafic rocks: implications for fluid sources and mobility in the subducted hydrous mantle. Contrib. Mineral. Petrol. 141, 145–159.

Gong, B., Zheng, Y.-F., Chen, R.-X., 2007. TC/EA-MS online determination of hydrogen isotope composition and water concentration in eclogitic garnet. Phys. Chem. Miner. 34, 687–698.

Hart, S.R., Zindler, A., 1986. In search of a bulk-Earth composition. Chem. Geol. 57, 247–267.

Hattori, K.H., Guillot, S., 2007. Geochemical character of serpentinites associated with high- to ultrahigh-pressure metamorphic rocks in the Alps, Cuba, and the Himalayas: recycling of elements in subduction zones. Geochem. Geophys. Geosyst. 8. https://doi.org/10.1029/2007GC001594.

Holland, T., Powell, R., 1996. Thermodynamics of order-disorder in minerals. 2. Symmetric formalism applied to solid solutions. Am. Mineral. 81, 1425–1437.

Holland, T.J.B., Powell, R., 1998. An internally consistent thermodynamic data set for phases of petrological interest. J. Metamorph. Geol. 16, 309–343.

Holland, T., Baker, J., Powell, R., 1998. Mixing properties and activity-composition relationships of chlorites in the system MgO-FeO-$Al_2O_3$-$SiO_2$-$H_2O$. Eur. J. Mineral. 10, 395–406.

Ishii, T., Robinson, P.T., Maekawa, H., Fiske, R., 1992. Petrological studies of peridotites from diapiric serpentinite seamounts in the Izu-Ogasawara-Mariana forearc. In: Fryer, P., Pearce, J.A., Stokking, L.B. (Eds.), Proceedings of the Ocean Drilling Program. Scientific Results. Ocean Drilling Program, College Station, TX, pp. 445–485.

Jagoutz, E., Palme, H., Baddenhausen, H., Blum, K., Cendales, M., Dreibus, G., Spettel, B., Lorenz, V., Vanke, H., 1979. The abundance of major, minor and trace elements in the earth's mantle as derived from primitive ultramafic nodules. Geochim. Cosmochim. Acta 11, 2031–2050.

Klein, F., Bach, W., Jöns, N., McCollom, T., Moskowitz, B., Berquó, T., 2009. Iron partitioning and hydrogen generation during serpentinization of abyssal peridotites from 15°N on the Mid-Atlantic Ridge. Geochim. Cosmochim. Acta 73, 6868–6893.

Klein, F., Bach, W., McCollom, T.M., 2013. Compositional controls on hydrogen generation during serpentinization of ultramafic rocks. Lithos 178, 55–69.

Klein, F., Bach, W., Humphris, S.E., Kahl, W.-A., Joens, N., Moskowitz, B., Berquo, T.S., 2014. Magnetite in seafloor serpentinite-Some like it hot. Geology 42, 135–138.

Kodolányi, J., Pettke, T., 2011. Loss of trace elements from serpentinites during fluid assisted transformation of chrysotile to antigorite-an example from Guatemala. Chem. Geol. 284, 351–362.

Kodolányi, J., Pettke, T., Spandler, C., Kamber, B.S., Gméling, K., 2012. Geochemistry of ocean floor and fore-arc serpentinites: constraints on the ultramafic input to subduction zones. J. Petrol. 53, 235–270.

Kyser, T.K., O'Hanley, D.S., Wicks, F.J., 1999. The origin of fluids associated with serpentinization processes: evidence from stable-isotope compositions. Can. Mineral. 37, 223–237.

Lafay, R., Deschamps, F., Schwartz, S., Guillot, S., Godard, M., Debret, B., Nicollet, C., 2013. High-pressure serpentinites, a trap-and-release system controlled by metamorphic conditions: example from the Piedmont zone of the western Alps. Chem. Geol. 343, 38–54.

Li, X.-P., Rahn, M., Bucher, K., 2004. Serpentinites of the Zermatt–Saas ophiolite complex and their texture evolution. J. Metamorph. Geol. 22, 159–177.

López Sánchez-Vizcaíno, V., Trommsdorff, V., Gómez-Pugnaire, M.T., Garrido, C.J., Müntener, O., Connolly, J.A.D., 2005. Petrology of titanian clinohumite and olivine at the high-pressure breakdown of antigorite serpentinite to chlorite harzburgite (Almirez Massif, S. Spain). Contrib. Mineral. Petrol. 149, 627–646.

Marchesi, C., Garrido, C.J., Padrón-Navarta, J.A., Sánchez-Vizcaíno, V.L., GómezPugnaire, M.T., 2013. Element mobility from seafloor serpentinization to high-pressure dehydration of antigorite in subducted serpentinite: insights from the Cerro del Almirez ultramafic massif (southern Spain). Lithos 178, 128–142.

Mattey, D., Lowry, D., Macpherson, C.G., 1994. Oxygen isotope composition of mantle peridotite. Earth Planet. Sci. Lett. 128, 231–241.

McDonough, W.F., Sun, S.-S., 1995. The composition of the Earth. Chem. Geol. 120, 223–253.

Mellini, M., Rumori, C., Viti, C., 2005. Hydrothermally reset magmatic spinels in retrograde serpentinites: formation of "ferritchromite" rims and chlorite aureoles. Contrib. Mineral. Petrol. 149, 266–275.

Merkulova, M.V., Muñoz, M., Vidal, O., Brunet, F., 2016. Role of iron content on serpentinite dehydration depth in subduction zones: experiments and thermodynamic modeling. Lithos 264, 441–452.

Merkulova, M.V., Muñoz, M., Brunet, F., Vidal, O., Hattori, K., Vantelon, D., Trcera, N., Huthwelker, T., 2017. Experimental insight into redox transfer by iron- and sulfur-bearing serpentinite dehydration in subduction zones. Earth Planet. Sci. Lett. 479, 133–143.

Niu, Y., 2004. Bulk-rock major and trace-element compositions of abyssal peridotites: implications for mantle melting, melt extraction and post-melting processes beneath mid-ocean ridges. J. Petrol. 45, 2423–2458.

Nozaka, T., 2003. Compositional heterogeneity of olivine in thermally metamorphosed serpentinite from Southwest Japan. Am. Mineral. 88, 1377–1384.

Nozaka, T., 2005. Metamorphic history of serpentinite mylonites from the Happo ultramafic complex, central Japan. J. Metamorph. Geol. 23, 711–723.

Padrón-Navarta, J.A., López Sánchez-Vizcaíno, V., Garrido, C.J., Gómez-Pugnaire, M.T., 2011. Metamorphic record of high-pressure dehydration of antigorite serpentinite to chlorite harzburgite in a subduction setting (Cerro del Almirez, Nevado– Filábride Complex, Southern Spain). J. Petrol. 52, 2047–2078.

Padrón-Navarta, J.A., López Sánchez-Vizcaíno, V., Hermann, J., Connolly, J.A.D., Garrido, C.J., Gómez-Pugnaire, M.T., Marchesi, C., 2013. Tschermak's substitution in antigorite and consequences for phase relations and water liberation in high-grade serpentinites. Lithos 178, 186–196.

Parkinson, I.J., Pearce, J.A., 1998. Peridotites from the Izu-Bonin-Mariana forearc (ODP Leg 125): evidence for mantle melting and melt-mantle interaction in a suprasubduction zone setting. J. Petrol. 39, 1577–1618.

Paulick, H., Bach, W., Godard, M., De Hoog, J.C.M., Suhr, G., Harvey, J., 2006. Geochemistry of abyssal peridotites (Mid-Atlantic Ridge, 15°20′N, ODP Leg 209): implications for fluid/rock interaction in slow spreading environments. Chem. Geol. 234, 179–210.

Pearce, J.A., Barker, P.F., Edwards, S.J., Parkinson, I.J., Lear, P.T., 2000. Geochemistry and tectonic significance of peridotites from the South Sandwich arc-basin system, South Atlantic. Contrib. Mineral. Petrol. 139, 36–53.

Pelletier, L., Müntener, O., Kalt, A., Vennemann, T.W., Belgya, T., 2008. Emplacement of ultramafic rocks into the continental crust monitored by light and other trace elements: an example from the Geisspfad body (Swiss-Italian Alps). Chem. Geol. 255, 143–159.

Peters, D., Bretscher, A., John, T., Scambelluri, M., Pettke, T., 2017. Fluid-mobile elements in serpentinites: Constraints on serpentinisation environments and element cycling in subduction zones. Chem. Geol. 466, 654–666.

Rebay, G., Spalla, M.I., Zanoni, D., 2012. Interaction of deformation and metamorphism during subduction and exhumation of hydrated oceanic mantle: Insights from the Western Alps. J. Metamorph. Geol. 30, 687–702.

Ren, Y., Chen, D., Hauzenberger, C., Liu, L., Liu, X., Zhu, X., 2016. Petrology and geochronology of ultrahigh-pressure granitic gneiss from South Dulan, North Qaidam belt, NW China. Int. Geol. Rev. 58, 171–195.
Rinaudo, C., Gastaldi, D., Belluso, E., 2003. Characterization of chrysotile, antigorite and lizardite by FT-Raman spectroscopy. Can. Mineral. 41, 883–890.
Rouméjon, S., Cannat, M., Agrinier, P., Godard, M., Andreani, M., 2015. Serpentinization and fluid pathways in tectonically exhumed peridotites from the Southwest Indian Ridge (62–65°E). J. Petrol. 56, 703–734.
Rouméjon, S., Früh-Green, G.L., Orcutt, B.N., Party, I.E.S., 2018. Alteration Heterogeneities in Peridotites Exhumed on the Southern Wall of the Atlantis Massif (IODP Expedition 357). J. Petrol. 59, 1329–1358.
Rüpke, L.H., Morgan, J.P., Hort, M., Connolly, J.A.D., 2004. Serpentine and the subduction zone water cycle. Earth Planet. Sci. Lett. 223, 17–34.
Saccocia, P.J., Seewald, J.S., Shanks, W.C., 2009. Oxygen and hydrogen isotope fractionation in the serpentine-water and talc-water systems from 250 to 450 °C, 50 MPa. Geochim. Cosmochim. Acta 73, 6789–6804.
Salters, V.J.M., Stracke, A., 2004. Composition of the depleted mantle. Geochem. Geophys. Geosyst. 5 (5). https://doi.org/10.1029/2003GC000597.
Scambelluri, M., Tonarini, S., 2012. Boron isotope evidence for shallow fluid transfer across subduction zones by serpentinized mantle. Geology 40, 907–910.
Scambelluri, M., Hoogerduijn-Strating, E.H., Piccardo, G.B., Vissers, R.L.M., Rampone, E., 1991. Alpine olivine- and titanian clinohumite-bearing assemblages in the Erro-Tobbio peridotite (Voltri Massif, NW Italy). J. Metamorph. Geol. 9, 79–91.
Scambelluri, M., Piccardo, G.B., Philippot, P., Robbiano, A., Negretti, L., 1997. High salinity fluid inclusions formed from recycled seawater in deeply subducted alpine serpentinite. Earth Planet. Sci. Lett. 148, 485–500.
Scambelluri, M., Bottazzi, P., Trommsdorff, V., Vannucci, R., Hermann, J., GòmezPugnaire, M.T., Lòpez-Sànchez Vizcaino, V., 2001. Incompatible element-rich fluids released by antigorite breakdown in deeply subducted mantle. Earth Planet. Sci. Lett. 192, 457–470.
Scambelluri, M., Fiebig, J., Malaspina, N., Muntener, O., Pettke, T., 2004a. Serpentinite subduction: implications for fluid processes and trace-element recycling. Int. Geol. Rev. 46, 595–613.
Scambelluri, M., Müntener, O., Ottolini, L., Pettke, T.T., Vannucci, R., 2004b. The fate of B, Cl and Li in the subducted oceanic mantle and in the antigorite breakdown fluids. Earth Planet. Sci. Lett. 222, 217–234.
Scambelluri, M., Pettke, T., Cannaò, E., 2015. Fluid-related inclusions in Alpine high-pressure peridotite reveal trace element recycling during subduction-zone dehydration of serpentinized mantle (Cima di Gagnone, Swiss Alps). Earth Planet. Sci. Lett. 429, 45–59.
Schmidt, M.W., Poli, S., 1998. Experimentally based water budgets for dehydrating slabs and consequences for arc magma generation. Earth Planet. Sci. Lett. 163, 361–379.
Schwartz, S., Guillot, S., Reynard, B., Lafay, R., Debret, B., Nicollet, C., Lanari, P., Auzende, A.L., 2013. Pressure-temperature estimates of the lizardite/antigorite transition in high pressure serpentinites. Lithos 178, 197–210.
Scicchitano, M.R., Rubatto, D., Hermann, J., Shen, T.T., Padrón-Navarta, J.A., Williams, I.S., Zheng, Y.-F., 2018. In situ oxygen isotope determination in serpentine minerals by ion microprobe: reference materials and applications to ultrahigh-pressure serpentinites. Geostand. Geoanal. Res. 42, 459–479.
Shen, T.T., Hermann, J., Zhang, L.F., Lü, Z., Padrón-Navarta, J.A., Xia, B., Bader, T., 2015. UHP metamorphism documented in Ti-chondrodite- and Ti-clinohumite-bearing serpentinized ultramafic rocks from Chinese southwestern Tianshan. J. Petrol. 56, 1425–1458.
Shi, R.D., Griffin, W.L., O'Reilly, S.Y., Zhao, G.C., Huang, Q.S., Li, J., Xu, J.F., 2010. Evolution of the Lüliangshan garnet peridotites in the North Qaidam UHP belt, Northern Tibetan Plateau: constraints from Re-Os isotopes. Lithos 117, 307–321.
Singer, B.S., Jicha, B.R., Leeman, W.R., Rogers, N.W., Thirlwall, M.F., Ryan, J., Nicolaysen, K.E., 2007. Along-strike trace element and isotopic variation in Aleutian island arc basalt: subduction melts sediments and dehydrates serpentine. J. Geophys. Res. 112, B06206. https://doi.org/10.1029/2006JB004897.
Snow, J.E., Dick, H.J.B., 1995. Pervasive magnesium loss by marine weathering of peridotite. Geochim. Cosmochim. Acta 59, 4219–4235.
Song, S.G., Su, L., Niu, Y., Zhang, L.F., 2007. Petrological and geochemical constraints on the origin of garnet peridotite in the North Qaidam ultrahigh-pressure metamorphic belt, Northwestern China. Lithos 96, 243–265.
Song, S.G., Niu, Y.L., Zhang, G.B., Zhang, L.F., 2009. Two types of peridotite in North Qaidam UHPM belt and their tectonic implications for oceanic and continental subduction: a review. J. Asian Earth Sci. 35, 285–297.
Song, S.G., Niu, Y.L., Su, L., Zhang, C., Zhang, L.F., 2014. Continental orogenesis from ocean subduction, continent collision/subduction, to orogen collapse, and orogen recycling: the example of the North Qaidam UHPM belt, NW China. Earth-Sci. Rev. 129, 59–84.
Spandler, C., Pirard, C., 2013. Element recycling from subducting slabs to arc crust: A review. Lithos 170–171, 208–223.
Spandler, C., Pettke, T., Hermann, J., 2014. Experimental study of trace element release during ultrahigh- pressure serpentinite dehydration. Earth Planet. Sci. Lett. 391, 296–306.
Sun, S.S., McDonough, W.F., 1989. Chemical and isotopic systematics of oceanic basalts: implications for mantle composition and processes. Geol. Soc. Lond. Spec. Publ. 42, 313–345.
Tenthorey, E., Hermann, J., 2004. Composition of fluids during serpentinite breakdown in subduction zones: evidence for limited boron mobility. Geology 32, 865–886.
Tonarini, S., Leeman, W.P., Leat, P.T., 2011. Subduction erosion of forearc mantle wedge implicated in the genesis of the South Sandwich Island (SSI) arc: Evidence from boron isotope systematics. Earth Planet. Sci. Lett. 301, 275–284.
Trommsdorff, V., Lòpez Sànchez-Vizcaíno, V.L., Gómez-Pugnaire, M.T., Müntener, O., 1998. High pressure breakdown of antigorite to spinifex-textured olivine and orthopyroxene, SE Spain. Contrib. Mineral. Petrol. 132, 139–148.
Ulmer, P., Trommsdorff, V., 1995. Serpentine stability to mantle depths and subduction-related magmatism. Science 268, 858–861.
Valley, J.W., Kitchen, N., Kohn, M.J., Niendorf, C.R., Spicuzza, M.J., 1995. UWG-2, a garnet standard for oxygen isotope ratio: strategies for high precision and accuracy with laser heating. Geochim. Cosmochim. Acta 59, 5223–5231.
Walter, M.J., 2003. Melt extraction and compositional variability in mantle lithosphere. In: Carlson, R.W. (Ed.), Treatise on Geochemistry, the Mantle and Core. 2. Elsevier, Amsterdam, pp. 363–394.
Warren, J.M., 2016. Global variations in abyssal peridotite compositions. Lithos 248–251, 193–219.
Wenner, D.B., Taylor, H.P.J., 1973. Oxygen and hydrogen isotopic studies of the serpentinization of ultramafic rocks in oceanic environments and continental ophiolite complexes. Am. J. Sci. 273, 207–239.
Wenner, D.B., Taylor, J.H.P., 1974. D/H and $O^{18}/O^{16}$ studies of serpentinization of ultramafic rocks. Geochim. Cosmochim. Acta 38, 1255–1286.
Whitney, D.L., Evans, B.W., 2010. Abbreviations for names of rock-forming minerals. Am. Mineral. 95, 185–187.
Wunder, B., Schreyer, W., 1997. Antigorite: high-pressure stability in the system MgO–$SiO_2$–$H_2O$ (MSH). Lithos 41, 213–227.
Xiong, Q., Griffin, W.L., Zheng, J.P., O'Reilly, S.Y., Pearson, N.J., 2015. Episodic refertilization and metasomatism of Archean mantle: evidence from an orogenic peridotite in North Qaidam (NE Tibet, China). Contrib. Mineral. Petrol. 169, 31.
Yang, J.J., Powell, R., 2008. Ultrahigh-pressure garnet peridotites from the devolatilization of sea-floor hydrated ultramafic rocks. J. Metamorph. Geol. 26, 695–716.
Zhang, G.B., Song, S.G., Zhang, L.F., Niu, Y.L., 2008. The subducted oceanic crust within continental-type UHP metamorphic belt in the North Qaidam, NW China: evidence from petrology, geochemistry and geochronology. Lithos 104, 99–118.
Zhang, G.B., Zhang, L.F., Song, S.G., 2009. UHP metamorphic evolution and SHRIMP geochronologyof a meta-ophiolitic gabbro in the North Qaidam, NW China. J. Asian Earth Sci. 35, 310–322.
Zhang, L., Chen, R.-X., Zheng, Y.-F., Li, W.-C., Hu, Z., Yang, Y., Tang, H., 2016. The tectonic transition from oceanic subduction to continental subduction: Zirconological constraints from two types of eclogites in the North Qaidam orogen, northern Tibet. Lithos 244, 122–139.
Zhang, J., Yu, S., Mattinson, C.G., 2017a. Early Paleozoic polyphase metamorphism in northern Tibet, China. Gondwana Res. 41, 267–289.
Zhang, L., Chen, R.-X., Zheng, Y.-F., Hu, Z., Xu, L., 2017b. Whole-rock and zircon geochemical distinction between oceanic- and continental-type eclogites in the North Qaidam orogen, northern Tibet. Gondwana Res. 44, 67–88.
Zheng, Y.-F., Wang, Z.-R., Li, S.G., Zhao, Z.-F., 2002. Oxygen isotope equilibrium between eclogite minerals and its constraint on mineral Sm–Nd chronometer. Geochim. Cosmochim. Acta 66, 625–634.